nature communications

Article

https://doi.org/10.1038/s41467-025-56703-2

CD248-targeted BBIR-T cell therapy against late-activated fibroblasts in cardiac repair after myocardial infarction

Received: 3 November 2023

Accepted: 24 January 2025

Published online: 27 March 2025

Check for updates

Haiting Chen[1,2,6], Ke Hu[1,6], Qi Tang[3,6], Junzhuo Wang[2], Qianyu Gu[2], Jiayu Chen[1], Jiaxin Hu[4], Ningxin Peng[1], Meng Guo[2], Yaohui Jiang[2], Qingbo Xu[5] ✉ & Jun Xie[1,2] ✉

Excessive cardiac fibrosis is a key cause of heart failure and adverse ventricular remodeling after myocardial infarction. The abnormally activated fibroblasts after scar maturation are the chief culprit. Single-cell RNA sequencing of mouse cardiac interstitial cells after myocardial infarction depicts a late-activated fibroblast subpopulation F-Act and initially identifies its characteristic antigen CD248, which is also verified in human hearts. On this basis, we develop a CD248-targeted biotin-binding immune receptor T cell therapy against F-Act to correct cardiac repair disorders. In our study, the precise removal of F-Act after the scar matured effectively inhibits fibrotic expansion in the peri-infarct zone and improves cardiac function. This therapy provides an idea for the treatment of cardiac fibrosis and also promotes the application of engineered T cells to non-tumor diseases.

Myocardial infarction (MI) is still the leading cause of mortality worldwide[1]. Most patients suffer from cardiac remodeling and heart failure in the chronic stage of MI[2]. Myocardial fibrosis is the prominent pathological phenotype in cardiac remodeling[3]. To date, there is no therapy to target excessive fibrosis directly in clinical practice, despite the large burden of the disease across the population.

The mechanism of temporal-spatial activation of fibroblasts post-MI is complex and sophisticated. The beneficial effects of fibroblasts in early infarct healing and the detrimental effects of excessive amounts of fibroblasts in uninjured tissue coexisted in the myocardium. Myofibroblasts, termed both αSMA-positive and periostin-positive fibroblasts, were beneficial in scar formation and remained silent after the scar maturation. Periostin-positive but αSMA-negative fibroblasts, identified as the activated fibroblast subpopulation F-Act, kept activated until the scar maturation, deposited collagen in the peri-infarct zone, and contributed to excessive cardiac fibrosis[4]. A previous study demonstrated that genetic ablation of *Postn*-positive fibroblasts 14 days after MI could reduce fibrosis and improve cardiac function in mice[5], indicating that F-Act is a potential therapeutic target in anti-fibrosis treatment. Recently, Aghajanian et al. reported that T cells with a chimeric antigen receptor (CAR) against fibroblast activation protein (FAP) could eliminate fibroblasts and attenuate cardiac fibrosis in mouse cardiac fibrosis models of transverse aortic constriction and angiotensin II infusion[6]. Nevertheless, FAP was also expressed in myofibroblasts and other beneficial subpopulations, indicating that it is not a suitable target for pathological cardiac fibroblasts in the condition of MI[7].

In this study, we performed a single-cell RNA sequencing (scRNA-seq) analysis of cardiac interstitial cells of the infarcted mice and further identified CD248 as the characteristic target antigen of F-Act. To eliminate this abnormally activated fibroblast subpopulation after the reparative scar of MI matures, we designed a bio-controllable biotin-

[1]Department of Cardiology, National Cardiovascular Disease Regional Center for Anhui, the First Affiliated Hospital of Anhui Medical University, No.218 Jixi Road, Hefei, Anhui 230022, China. [2]Affiliated Drum Tower Hospital, Medical School, Nanjing University, No.321 Zhongshan Road, Nanjing, Jiangsu 210008, China. [3]NHC Key Laboratory of Antibody Technique, Nanjing Medical University, No.101 Longmian Road, Nanjing, Jiangsu 211166, China. [4]Cardiovascular Disease Center, The Central Hospital of Enshi Tujia and Miao Autonomous Prefecture, Enshi Clinical College of Wuhan University, No.158 Wuyang Road, Enshi, Hubei 445099, China. [5]Department of Cardiology, the First Affiliated Hospital, Zhejiang University School of Medicine, No.79 Qingchun Road, Hangzhou, Zhejiang 310003, China. [6]These authors contributed equally: Haiting Chen, Ke Hu, Qi Tang. ✉e-mail: qingbo_xu@zju.edu.cn; xiejun@ahmu.edu.cn

binding immune receptor (BBIR)-T cell therapy referring to the reported universal CAR-T strategy[8]. The BBIR comprises an extracellular modified dimeric avidin (dcAv) to an intracellular T cell signaling domain. BBIR-T cell recognized and bound exclusively to F-Act pre-labeled with specific biotinylated molecules that we here employed biotinylated anti-CD248 F(ab')2 (abbreviated as "BF"). The administration of the BBIR-T cell therapy to the mouse MI model was divided into two steps. Firstly, the CD248-positive F-Act in the injured myocardium was labelled with BF by intramyocardial injection immediately after MI surgery. Then, from 14 days post-MI, BBIR-T cells were injected intravenously to kill F-Act when the infarct scar almost matured. The therapeutic effects of the BBIR-T cell therapy on cardiac fibrosis and remodeling after MI were assessed with cultured fibroblasts and an animal model. This study demonstrated that BBIR-T cell treatment after two weeks post-MI could significantly delay the deterioration of cardiac function. This study sheds light on a promising and clinically translational therapy against cardiac fibrosis after MI and an application of engineered T cells to non-tumor diseases.

Results

Identification of cardiac fibroblast subpopulation F-Act

To illustrate the cellular characteristics of fibroblasts after MI, we performed a scRNA-seq of the cardiac interstitial cell population in the ischemic myocardium using the 10X Genomics Chromium platform at the 7th and 14th day post-sham or post-MI surgery. The transcriptional profile of 13441 cells was captured after quality control filtering. We performed unbiased clustering on an aggregate of cells using the Seurat R package[9] to identify cells with distinct lineage identities and transcriptional states, with cell populations visualized in uniform manifold approximation projection (UMAP) dimensionality reduction plots.

The cardiac interstitial cells were represented by a total of 9 distinct cell lineages (Fig. 1a), with the most significant proportion of fibroblasts (*Col1a1*$^+$*Pdgfra*$^+$, 6118, 45.5%), followed by endothelial cells (*Kdr*$^+$*Pecam1*$^+$, 4371, 32.5%) and macrophages (*Cd68*$^+$*Itgam*$^+$, 1898, 14.1%). For further clustering analysis of fibroblasts, we observed 11 subpopulations (Fig. 1a, Supplementary Fig. 1a, b). F-SH was characterized by high expression of *Sca1*, a stem/progenitor cell marker enriched in the uninjured adult mice with multilineage differentiation and self-renewal potential[9,10](Supplementary Fig. 1c). F-MFC represents matrifibrocytes, which were characterized by high expression of *Comp* and mainly distributed in the myocardial scars and play a functional role in maintaining the integrity of the mature scar[11–13]. Myofibroblasts, termed as F-Myo, increased significantly after 7 days post-MI and showed a strong upregulation of numerous collagen genes (*Col1a1*, *Col3a1*, and *Col5a1*), as well as *Postn* and *Acta2* at a high level (Fig. 1b, Supplementary Fig. 1d), indicative of activated state and contractile phenotype[14–16]. Interestingly, in addition to F-Myo, another *Postn*-positive fibroblast subpopulation was termed as F-Act and distinguished from F-Myo by low *Acta2* expression (Fig. 1b)[10]. Gene ontology (GO) enrichment analysis in the categories of biological processes (BP), molecular functions (MF), and cellular components (CC) revealed that the upregulated genes in F-Act were enriched in cell adhesion, extracellular matrix binding, and fibronectin binding (Supplementary Fig. 1e), indicating that F-Act was also activated and participated in collagen deposition.

To clarify the temporal-spatial distribution of F-Act and F-Myo, we performed the immunofluorescence (IF) staining for periostin and αSMA in the heart tissue at different time points after MI (Fig. 1c and Supplementary Fig. 1f, g). Periostin-positive fibroblasts (stained green) were mainly distributed in the infarct and peri-infarct zone but barely in the remote zone and persisted until 28 days post-MI. Among them, αSMA-positive (stained red) F-Myo was enriched in the infarct zone, which appeared on the 7th day, peaked on the 14th day post-MI, and gradually decreased[17]. At the same time, αSMA-negative F-Act was observed in the peri-infarct zone from 7 days post-MI and maintained until 28 days, indicating that F-Act was persistently activated after scar maturation and might be a critical etiological factor in abnormal termination of fibrosis after MI.

To further examine the quantitative dynamic changes of F-Act after MI, Pdgfrα reporter mice (Pdgfra-CRE:tdTomato) were generated to trace cardiac interstitial fibroblasts. The proportion of the F-Act in cardiac fibroblasts at different time points after MI was detected by flow cytometry (Fig. 1d). In the hearts of uninjured adult mice, pdgfrα-positive cardiac fibroblasts account for approximately 5–10%. In the injured myocardium, the percentage of pdgfrα-positive fibroblasts, mainly periostin-positive fibroblasts, increased significantly after MI, peaked at about 50% on the 14th day post-MI, and then gradually decreased, indicating that a large number of fibroblasts were activated and proliferated for tissue repair and became quiescent or underwent apoptosis after scar formation[18,19]. F-Myo predominated in the first two weeks after MI and gradually dropped to the baseline level on the 28th day post-MI. In comparison, F-Act progressively increased from the 7th day to at least the 28th day post-MI. F-Act began to surpass F-Myo to become the dominant fibroblast subpopulation on the 21st day post-MI.

To further clarify the heterogeneity of the F-Act and F-Myo subpopulations, we conducted stereo-seq on mouse hearts from both sham and 10-day post-MI groups. To investigate the spatial distribution of F-Act and F-Myo based on spatial transcriptome data, we selected the top 10 marker genes based on the scRNA-seq data to define the marker gene sets for each fibroblast subpopulation, ensuring that there was nearly no overlap between the marker sets, thus confirming the uniqueness of these cell populations. The spatial distribution of fibroblast subpopulations was then calculated using the 'AddModuleScore' function and visualized using the "SpatialFeaturePlot" function in Seurat[20], which maps the identified fibroblast subpopulations onto the tissue sections. This approach enabled the identification and spatial mapping of distinct cellular domains within the tissue, providing deeper insights into the spatial architecture and cellular composition of the sample. Our findings revealed that 10 days post-MI, the F-Act subpopulation is significantly more abundant than the F-Myo subpopulation in the heart, with the former primarily localized in the peri-infarct zone and the latter mainly within the infarcted zone. The F-Act and F-Myo subpopulations displayed distinct characteristics in terms of both quantity and spatial distribution, leading us to conclude that these two fibroblast subpopulations are independent entities. Notably, a minor population of F-Act was also detected in the undamaged regions of the remote zone, indicating that F-Act could infiltrate normal tissue (Fig. 1e). The timely elimination of F-Act cells may hold therapeutic potential for the repair of post-infarction injuries.

Taken together, we observed a subpopulation of cardiac fibroblasts termed F-Act that was persistently activated in the peri-infarct zone until scar maturation and became the dominant subpopulation on the 21st day post-MI.

Screening for the characteristic surface antigen of F-Act

Considering the pathological role of the F-Act, we aimed to employ the CAR-T cell immunotherapy to remove it precisely. Previous studies have used FAP as a fibroblast antigen for CAR-T cells[6,21] against cardiac fibrosis induced by angiotensin II and phenylephrine (AngII/PE). However, post-infarction cardiac fibrosis involves mechanisms different from other fibrotic diseases. Different fibroblast subpopulations have distinct roles and indiscriminate clearance of fibroblasts is detrimental to scar formation and stability. UMAP and violin plots showed that *Fap* is widely expressed in all fibroblast subpopulations, especially in the F-Myo subpopulation (Supplementary Fig. 2a). IF staining revealed that FAP-positive cells were co-localized with αSMA-positive cells (Supplementary Fig. 2b), and flow cytometry showed that the dynamic changes in the number of FAP-positive cells post-MI closely

https://doi.org/10.1038/s41467-025-56703-2

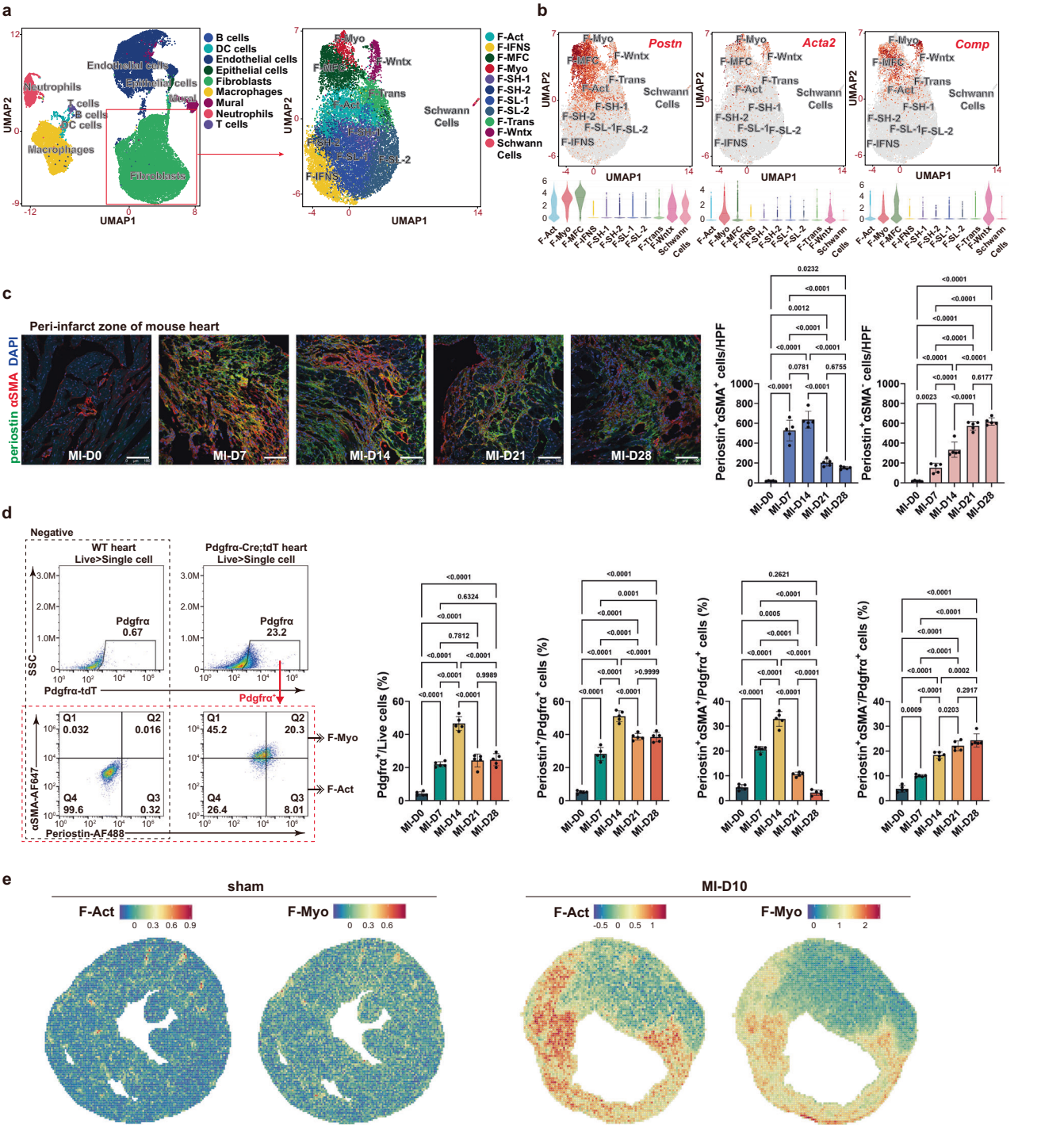

Fig. 1 | Identification of cardiac fibroblast subpopulation F-Act. a UMAP clustering of 13441 cardiac interstitial cells (left) and fibroblasts (right) isolated from C57BL/6 J wild-type (WT) mice at 7 and 14 days post-sham and post-MI surgery. Each dot represents a single cell. The expression of known marker genes annotated cell type. **b** UMAP and violin plots depict *Postn*, *Acta2*, and *Comp* expression in fibroblasts. **c** Triple IF staining for periostin (green) and αSMA (red) in the peri-infarct zone of the hearts of C57BL/6 J WT mice 0, 7, 14, 21, and 28 days after MI surgery. Nuclei were stained blue. Scale bar = 100 μm. Quantification of the number of periostin$^+$αSMA$^+$ F-Myo and periostin$^+$αSMA$^-$ F-Act in each high-power field (HPF). $n = 5$ mice at each time point after MI. **d** Flow cytometry of fibroblasts isolated from hearts of C57BL/6 J WT and Pdgfra-CRE:tdTomato mice. Total cardiac fibroblasts were lineage traced by pdgfrα. F-Myo and F-Act were marked with antibodies against periostin-AF488 and αSMA-AF647. Quantification of the pdgfrα$^+$ fibroblast ratio in live cells, periostin$^+$ fibroblasts ratio in pdgfrα$^+$ fibroblasts, periostin$^+$ αSMA$^+$ F-Myo ratio in pdgfrα$^+$ fibroblasts, and periostin$^+$ αSMA$^-$ F-Act ratio in pdgfrα$^+$ fibroblasts. $n = 5$ mice at each time point after MI. **e** Spatial distribution of the F-Act and F-Myo subpopulation in mouse heart sections from sham and 10 days post-MI conditions, visualized through the integration of scRNA-seq and stereo-seq methodologies. **c, d** Data are the mean ± SEM and *p*-values are displayed in the bar charts, one-way ANOVA followed by Tukey's multiple comparisons tests. Source data are provided as a Source Data file.

https://doi.org/10.1038/s41467-025-56703-2

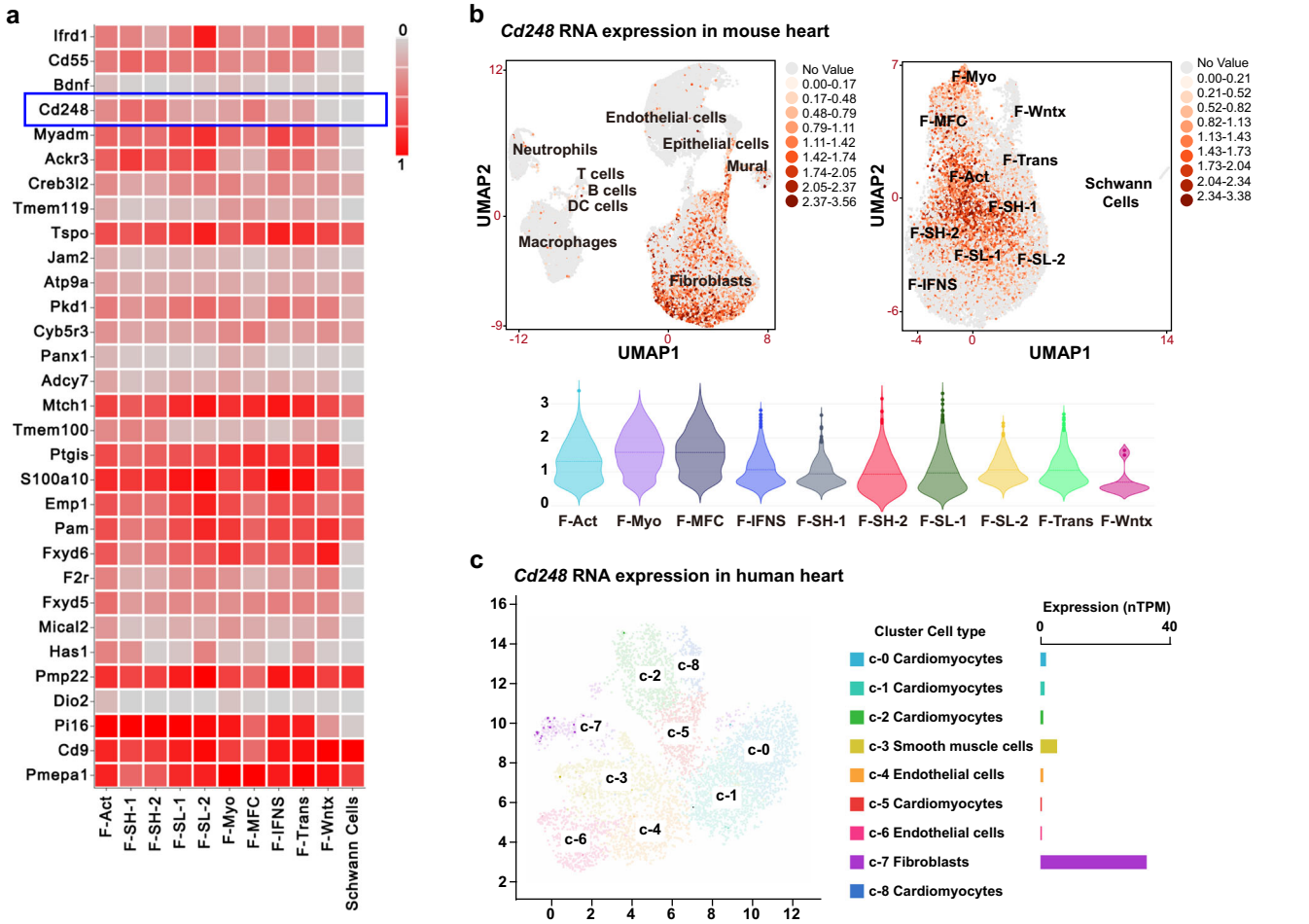

Fig. 2 | Screening for the characteristic surface antigen of F-Act. a Heatmap of genes highly expressed in the F-Act and encoding membrane proteins. **b** UMAP depicts *Cd248* expression in mouse cardiac interstitial cells (left) and fibroblasts (right). **c** UMAP depicts *Cd248* expression in human heart muscle in the HPA.

mirrored those of αSMA-positive F-Myo (Supplementary Fig. 2c). The continuation of FAP as a target for CAR-T cells inevitably harms other beneficial fibroblast subpopulations that form and stabilize myocardial scars, so exploring the F-Act-specific antigen markers is of great significance.

To identify surface proteins expressed specifically in the F-Act, we compared all genes encoding membrane proteins and highly expressed in the F-Act from scRNA-seq data, referring to the Human Protein Atlas (HPA) (Fig. 2a). Excluding genes highly expressed in F-Myo or F-MFC (e.g., *Pempa1* and *Pi16*) and those indiscriminately expressed in all fibroblast subpopulations (e.g., *Pmp22*, *Mtch1*, *Tspo*), *Cd248*, *Tmem100*, and *Ackr3* were picked out. However, given that *Ackr3* was also expressed in monocytes/macrophages and endothelial (Supplementary Fig. 2d) and *Tmem100* was functionally expressed in the lung(Supplementary Fig. 2e, f)[22], we finally focused on *Cd248*, which is highly expressed only in the fibroblast subpopulations F-Act and F-SH and almost not expressed in other major cardiac interstitial cell types (Fig. 2b).

CD248 is a type 1 transmembrane glycoprotein found on the plasma membrane of activated mesenchymal cells. CD248 functions only during embryonic development in the physiological state and is not expressed or found at deficient levels in adult tissues[23]. Alignment of the mouse and human amino acid sequences showed an overall 77.5% identity[24]. Protein and RNA expression overview from the human protein atlas (HPA) confirmed that CD248 was expressed mainly in the duodenum, adipose, small intestine, and moderately in the heart muscle (Supplementary Fig. 2g, h). The scRNA-seq of human heart muscle from HPA showed that *Cd248* was expressed mainly in fibroblasts, a small amount in smooth muscle cells, and barely in cardiomyocytes (Fig. 2c). As the evidence of the sequencing IF staining of healthy mouse liver, spleen, lung, and kidney showed that CD248 was expressed only in small amounts around vessels and was mainly colocalized with activated fibroblasts (periostin$^+$) and smooth muscle cells (αSMA$^+$) but not with endothelial cells (CD31$^+$), neutrophils (Ly6G$^+$), and macrophages (CD68$^+$) (Supplementary Fig. 3).

Identification of CD248 as the target antigen for CAR-T cells against F-Act

To demonstrate the specificity of CD248 as a characteristic antigen of the F-Act, we performed IF staining of mouse hearts at different time points after MI (Fig. 3a and Supplementary Fig. 4a). In the infarct and peri-infarct zone, CD248-positive (stained red) cells fused with periostin-positive (stained green) fibroblasts, and the proportion of double-positive cells continued to increase until 28 days after MI. At the same time, CD248-positive cells were rarely present in the remote zone of undamaged myocardium. Western blot analysis of the left ventricular and ventricular septal myocardium also showed that the protein expression of CD248 gradually increased over time after MI (Supplementary Fig. 4b). On the 14th day post-MI, CD248-positive cells coincided barely with αSMA-positive F-Myo and very little with COMP-positive F-MFC (Fig. 3b), demonstrating that CD248 was expressed in F-Act specifically and targeting CD248 to clear F-Act would not harm F-Myo and F-MFC.

Considering the high homology of mouse and human CD248 amino acid sequences, we performed IF staining of the heart sample

https://doi.org/10.1038/s41467-025-56703-2

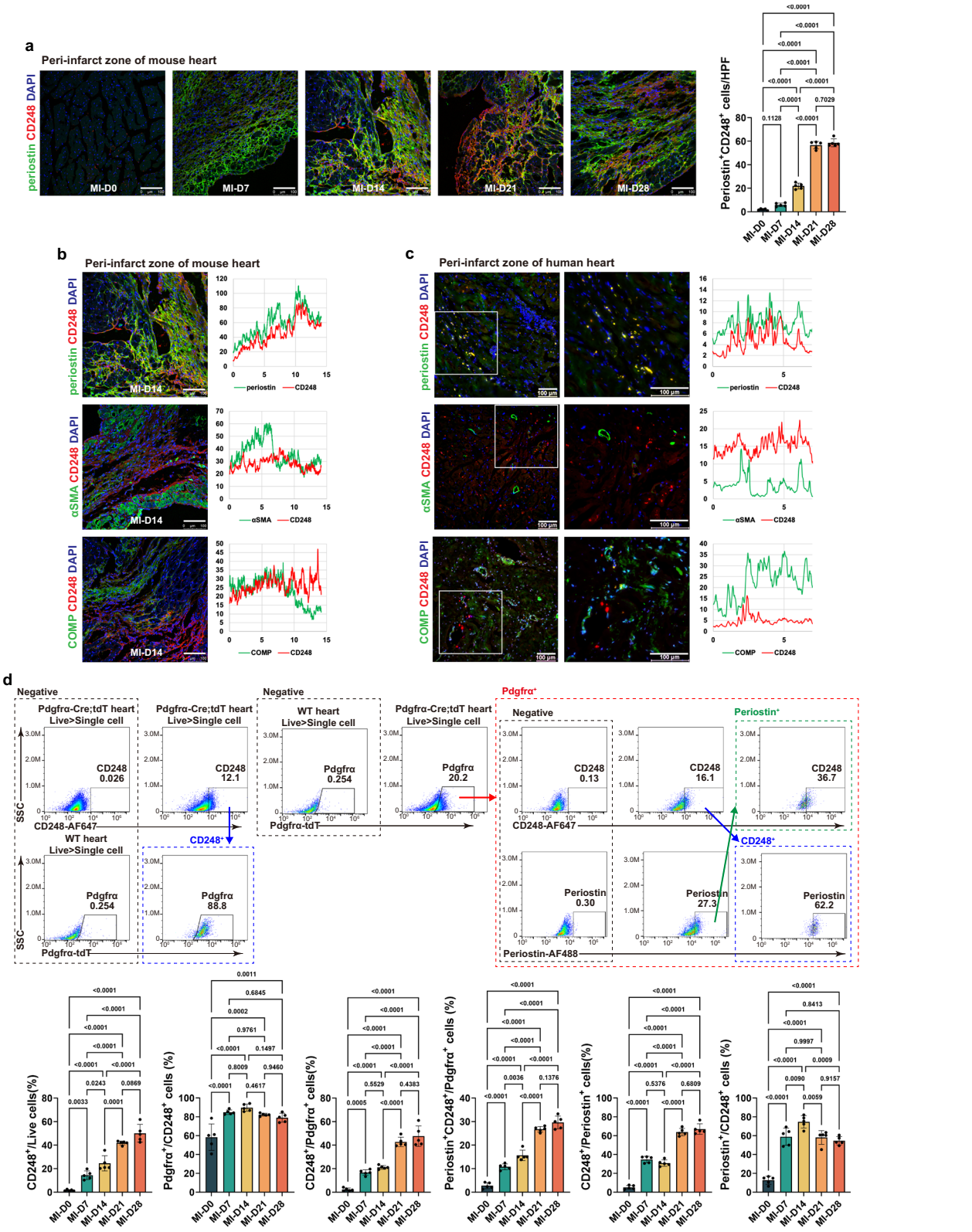

collected from the patient diagnosed with MI before heart transplantation. (Fig. 3c and Supplementary Fig. 4c). Consistent with the mouse MI model, CD248-positive cells were enriched in the infarct and peri-infarct zone and colocalized with periostin-positive fibroblasts. Still, they did not coincide with αSMA-positive F-Myo or COMP-positive F-MFC. Interestingly, a small amount of CD248-positive and periostin-positive F-Act was found in the remote zone of undamaged myocardium, suggesting that some fibroblasts may migrate from the infarct and peri-infarct zone to the uninjured remote zone.

Furthermore, we performed a flow cytometry assay on Pdgfra-CRE:tdTomato mouse hearts (Fig. 3d). After MI, the proportion of CD248-positive cells in all living cells and pdgfrα-positive fibroblasts gradually increased until the scar matured. From the 7th day post-MI, pdgfrα-positive fibroblasts accounted for more than 80% of CD248-positive cells, proving that CD248-positive cells were mainly

https://doi.org/10.1038/s41467-025-56703-2

Fig. 3 | Identification of CD248 as the target antigen for CAR-T cells against F-Act. a Triple IF staining for periostin (green) and CD248 (red) in the peri-infarct zone of the hearts of C57BL/6J WT mice 0, 7, 14, 21, and 28 days after MI surgery. Nuclei were stained blue. Scale bar = 100 μm. Quantification of the periostin$^+$CD248$^+$ cell to DAPI ratio in each HPF. $n = 5$ mice at each time point after MI. Triple IF staining of periostin, αSMA, COMP (stained green), and CD248 (stained red) in the hearts of MI mouses (**b**) and a patient with ischemic cardiomyopathy (**c**). Nuclei were stained blue. Scale bar =100 μm. IF staining of mouse heart was repeated in heart sections from 5 independent mice, while IF of human heart was repeated 5 times in heart sections from one patient with ischemic cardiomyopathy, yielding similar results. **d** Flow cytometry of cells isolated from hearts of C57BL/6J WT mouses and Pdgfra-CRE:tdTomato mice. Total cardiac fibroblasts were lineage traced by pdgfrα. Quantification of the CD248$^+$ cell ratio in live cells, pdgfrα$^+$ fibroblast ratio in CD248$^+$ cells, CD248$^+$ cell ratio in pdgfrα$^+$ fibroblasts, periostin$^+$CD248$^+$ cell ratio in pdgfrα$^+$ fibroblasts, CD248$^+$ cell ratio in periostin$^+$ activated fibroblasts, and periostin$^+$ activated fibroblasts in CD248$^+$ cells. $n = 5$ mice at each time point after MI. **a, d** Data are the mean ± SEM and *p*-values are displayed in the bar charts, one-way ANOVA followed by Tukey's multiple comparisons tests. Source data are provided as a Source Data file.

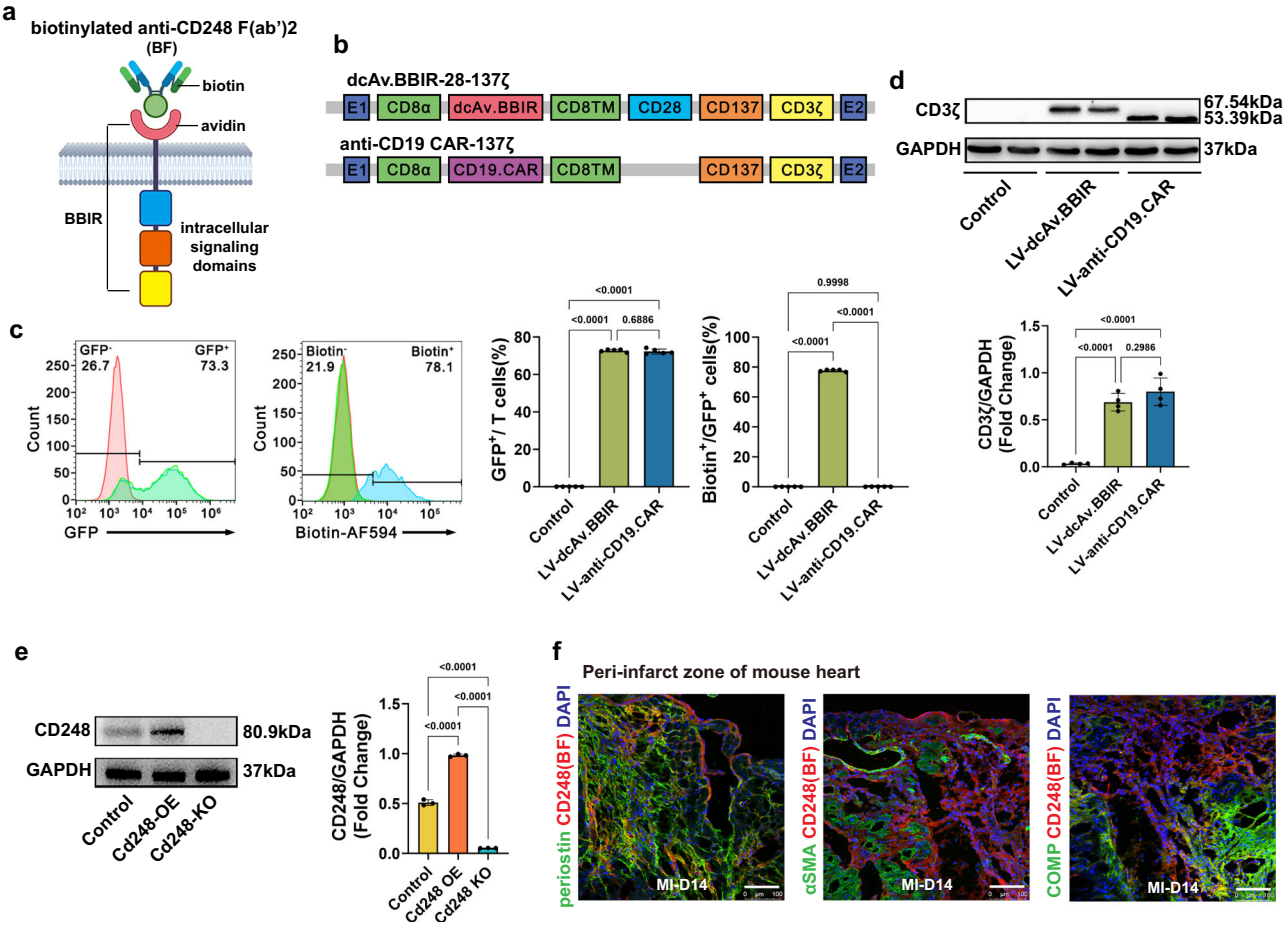

Fig. 4 | Construction and functional verification of the BBIR-T cell system targeting CD248. a Schematic diagram of the structure of the BBIR-T system. Created in BioRender. Haiting, C. (2025) https://BioRender.com/l46n352. **b** Schematic images of dcAv. BBIR-28-137ζ and CD19. CAR-137ζ sequence. **c** Western blotting shows exogenous CD3ζ expression in HEK-293T cells transduced with lentivirus (LV)-dcAv.BBIR and LV-anti-CD19.CAR. The samples derive from the same experiment and that gels/blots were processed in parallel. Quantifying the relative protein expression of CD3ζ to GAPDH. $n = 4$ cell culture wells of each group. **d** Flow cytometry of human peripheral T cells transduced with LV-dcAv.BBIR and LV-anti-CD19.CAR. Quantifying GFP$^+$ cells ratio to total T cells and biotin$^+$ cells ratio to GFP$^+$ cells. $n = 5$ cell culture wells of each group. **e** Western blotting by BF shows CD248 expression in NIH-3T3 cells with or without *Cd248* overexpression(OE) or knock-out(KO). The samples were derived from the same experiment and that gels/blots were processed in parallel. Quantifying the relative protein expression of CD248 to GAPDH. $n = 4$ cell culture wells of each group. **f** Triple IF staining of periostin, αSMA, COMP (green), and biotinylated anti-CD248 F(ab')2 (shorted as BF) (red) in the peri-infarct zone 14 days after MI surgery. Nuclei were stained blue. Scale bar =100 μm. Each experiment was repeated 5 times independently with similar results. **c-e** Data are the mean ± SEM and *p*-values are displayed in the bar charts, one-way ANOVA followed by Tukey's multiple comparisons tests. Source data are provided as a Source Data file.

fibroblasts. The dynamic trend of the number of CD248-positive cells in the process of MI was consistent with that of periostin-positive and αSMA-negative cells described above in Fig. 1d. Moreover, after 7 days post-MI, the proportion of periostin-positive cells in CD248-positive cells remained above 60%, indicating that most CD248-positive cells were activated.

In summary, the expression property of CD248 made it possible to be an effective and safe target antigen for the CAR-T cells against F-Act.

Construction and functional verification of the BBIR-T Cell system targeting CD248

Given that CD248 was expressed in some abdominal organs, we drew on previously reported BBIR-T cell strategy to optimize CAR-T cell therapy to reduce the off-target effect[8]. BBIR-T cells used dcAv as the extracellular T-cell domain, which could recognize and bind a variety of biotinylated antigen-specific molecules effectively linked to an intracellular T-cell signaling domain (Fig. 4a). We planned to label F-Act by intramyocardial injection of BF immediately after the MI surgery

https://doi.org/10.1038/s41467-025-56703-2

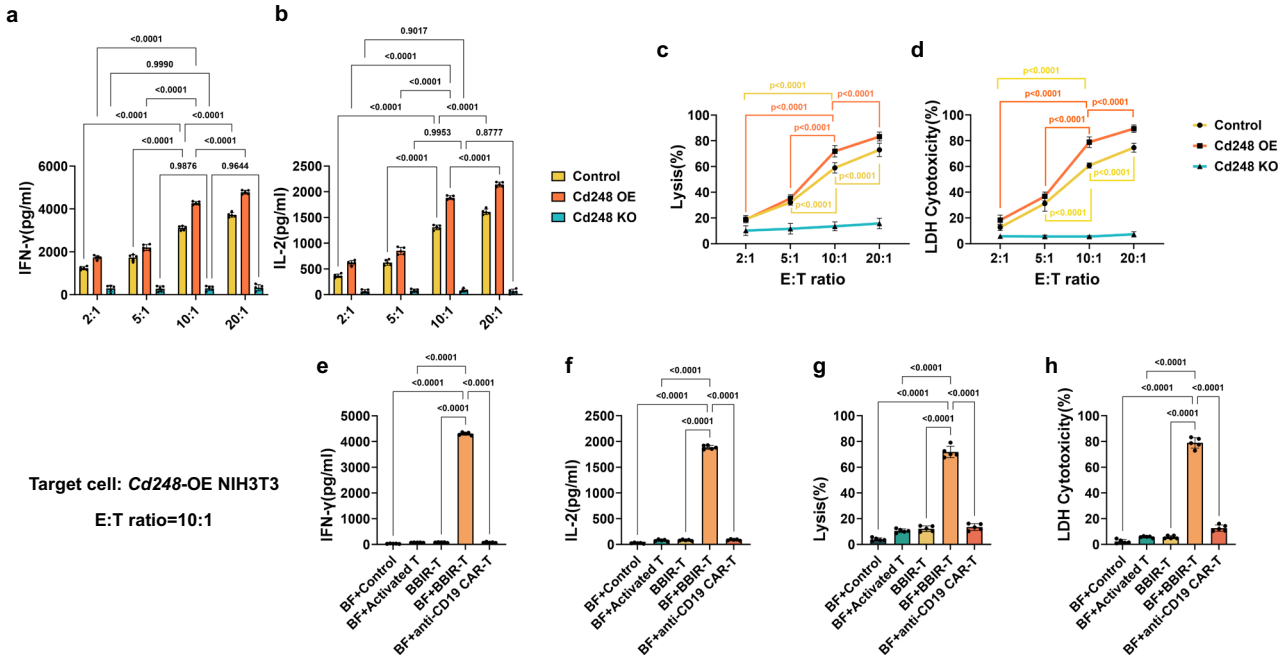

Fig. 5 | In vitro killing effect of BBIR-T cell therapy on CD248-positive fibroblasts. a-d BBIR-T cells were cocultured with BF-labelled NIH-3T3 cells with or without *Cd248* OE or KO. The E:T ratio =2:1, 5:1, 10:1, and 20:1. ELISA determined the secretion of IFN-γ (**a**) and IL-2 (**b**) in the supernatant 24 h after coculture. $n = 5$ cell culture wells of each group. Data are the mean ± SEM and *p*-values are displayed in the bar charts, two-way ANOVA followed by Dunnett's multiple comparison test. **c** Cell lysates were analyzed at 24 h after coculture by CCK-8 cell viability assay. **d** Cytotoxicity was measured by LDH activity in the supernatant 24 h after coculture. **c, d** Biological replicates ($n = 5$ cell culture wells) were conducted for each E:T ratio across different target cells. *P*-values less than 0.05 are displayed in the line charts, two-way ANOVA followed by Dunnett's multiple comparison test. **e–h** Different effector cells cocultured with *Cd248*-OE NIH-3T3 cells. E: T = 10:1. ELISA was used to determine the secretion of IFN-γ (**e**) and IL-2 (**f**) in the supernatant 24 h after coculture. **g** Cell lysates were analysed at 24 h after coculture by CCK-8 cell viability assay. **h** Cytotoxicity was measured by LDH activity in the supernatant 24 h after coculture. $n = 5$ cell culture wells of each group. Data are the mean ± SEM and *p*-values are displayed in the bar charts, one-way ANOVA followed by Dunnett's multiple comparison test. Source data are provided as a Source Data file.

and remove F-Act by intravenous injection of BBIR-T cells after the infarct scar matured. This therapy used biotinylated antigen-specific molecules as intermediaries to connect effector cells and target cells, which could limit the effect site of BBIR-T cells to the heart.

Figure 4b shows the gene constructs of BBIR containing dcAv fused to the human CD3ζ cytosolic domain in combination with the CD28 and CD137 costimulatory modules. While the independent anti-CD19 CAR containing anti-CD19 Fc fragment fused with CD3ζ and CD137 was constructed as a control. HEK-293T cells were transduced by transfer plasmids pdcAv.BBIR and panti-CD19.CAR containing green fluorescent protein (GFP) and stained with biotin labelled by fluorescein AF594. BBIR-293T cells could express avidin and exogenous CD3ζ and recognize and bind biotin (Supplementary Fig. 5a-c).

Human peripheral blood-derived T cells were used for in vitro functional verification, while mouse spleen-derived T cells were used for in vivo treatment. Flow cytometry showed that CD3-positive T cells accounted for more than 90% of all viable cells 5 days after extraction, of which CD4-positive and CD8-positive cells accounted for approximately 50% and 40%, respectively (Supplementary Fig. 5d). The transfer plasmids were packaged into lentiviruses to transduce T cells to prepare BBIR-T cells and anti-CD19 CAR-T cells. Flow cytometry showed that more than 70% lentivirus transduction efficiency could be achieved, and more than 70% of BBIR-T cells could recognize and bind biotin (Fig. 4c). Western blotting was used to detect the expression of exogenous CD3ζ in BBIR-T cells and anti-CD19 CAR-T cells (Fig. 4d).

To alleviate the immunogenicity of the whole antibodies[25], anti-CD248 F(ab')2 fragments were prepared through pepsin digestion and ultrafiltration purification (Supplementary Fig. 5e, f), which could be detected by anti-mouse IgG F(ab') secondary antibody (Supplementary Fig. 5g). Labeling anti-CD248 F(ab')2 with biotin enables it to be recognized by BBIR-T cells via a biotin-avidin bridge. Western blotting of CD248 using BF as the primary antibody demonstrated the specificity of this engineered antibody (Fig. 4e). Mouse heart IF showed that BF could recognize and bind CD248-positive cells, consistent with the results in Fig. 3, where labelled cells were mainly located in the infarct and peri-infarct zone, co-expressing periostin but not αSMA or COMP (Fig. 4f).

In vitro killing effect of BBIR-T cell therapy on CD248-positive fibroblasts

To verify the effectiveness of the BBIR-T cell therapy, we prepared target cells—the mouse embryonic fibroblast line NIH-3T3, which was previously reported to express CD248[24]. Overexpression (OE) or knockout (KO) of *Cd248* in NIH-3T3 cells was performed by lentivirus transduction and puromycin screening (Supplementary Fig. 6a-c). Target cells were labeled with BF and cocultured with effector cells—BBIR-T cells. The effector-to-target cell ratio (E:T ratio) gradient was set from 2:1 to 20:1. Cytokine secretion in the supernatant was detected 24 h after coculture by enzyme-linked immunosorbent assay (ELISA). The concentrations of IFN-γ and IL-2 in NIH-3T3 cells and *Cd248*-OE NIH 3T3 cells increased with increasing E:T ratio, indicating that BBIR-T cells were successfully activated (Fig. 5a, b). Cytotoxicity was detected by cell counting kit-8 (CCK-8) and lactic dehydrogenase (LDH) release experiments. When the E:T ratio reached 10:1, BBIR-T cells killed more than 80% of CD248-positive cells (Fig. 5c, d), so subsequent experiments used a fixed E:T ratio of 10:1. On the other hand, the BBIR-T system had no noticeable killing effect on *Cd248*-KO NIH 3T3 cells and did not lead to the activation of BBIR-T cells.

To demonstrate the safety of the BBIR-T cell therapy, we prepared different effector cells, including activated T cells, BBIR-T cells, and

anti-CD19 CAR-T cells. The cell experiments were divided into 5 groups: BF + Control, BF + Activated T, BBIR-T, BF + BBIR-T, and BF + anti-CD19 CAR-T. Most of the target cells were labeled with BF except for those in the BBIR-T group. The target cells in the BF + Control group were not cocultured with effector cells. At the same time, the target cells in the other group were cocultured with different effector cells for 24 h. By detecting the secretion of IFN-γ and IL-2 in the supernatant and target-cell cytotoxicity (Fig. 5e-h and Supplementary Fig. 6d-k), it was found that only in the BF + BBIR-T group, the T cells could be activated and clear NIH-3T3 cells as well as *Cd248*-OE NIH-3T3 cells, but had no effect on *Cd248*-KO NIH-3T3 cells. The above results showed that three conditions must be met simultaneously for the BBIR-T cell therapy: the target cell expressed CD248, the target cells were labelled by BF, and the effector cells were present as BBIR-T cells.

Three-time injections of BBIR-T cells improved the cardiac function of MI mice

Through IF monitoring of biotin in the myocardium, it was found that the intramyocardially injected BF can reside in the heart for at least 14 days (Supplementary Fig. 7b). To verify BF's feasibility in labelling CD248-positive cells in vivo, C57BL/6 J WT mouse was modelled for MI and BF was injected intramyocardial immediately after MI surgery. After 14 days, the mouse heart was obtained for IF staining of biotin and periostin. As shown in Supplementary Fig. 7a, biotin-positive cells could still be observed after 14 days of intramyocardial injection, and most of them were colocalized with periostin-positive cells.

To explore the injection regimen and the effect of the BBIR-T cell therapy in clearing F-Act in vivo, as shown in Fig. 6a, we performed MI surgery on Pdgfra-CRE:tdTomato mice and injected intramyocardially with BF into the infarcted myocardium immediately after the MI surgery. From the 14th day post-MI, 10^6 BBIR-T cells were injected into the tail vein every 3 days, and 5 mouse hearts were collected in batches 3 days after administration for flow cytometry detection (Fig. 6b). The results showed that the proportion of CD248-positive cells gradually decreased as the number of administrations increased. When BBIR-T cells were injected three times, CD248-positive cells decreased by approximately 2/3 and were not further reduced after the 4^{th} injection of BBIR-T cells. Therefore, follow-up treatment was administered with three intravenous injections.

The following animal experiments were designed to further validate the BBIR-T cell therapy's efficacy, as shown in Fig. 6c, d. The Pdgfra-CRE:tdTomato mice were divided into 6 groups. The sham group only opened the chest without ligating the left anterior descending (LAD); the remaining 5 groups underwent LAD ligation. Except for the sham and MI + BBIR group, the other groups were injected intramyocardially with BF immediately after MI. On the 14th, 17th, and 20th days post-MI, except for the sham and MI + BBIR groups, the other groups were injected intravenously with different effector cells. Ultrasound cardiogram (UCG) was performed before MI surgery and 7, 14, and 28 days after MI to evaluate cardiac systolic function and left ventricular movement. Mice were sacrificed after LV catheterization testing 28 days post-MI. Although mouse deaths in the MI + BF + BBIR-T group decreased after implementing the BBIR-T cell therapy, the Kaplan-Meier survival curve showed no statistical significance in 1-month survival between different MI groups (Supplementary Fig. 7c).

Echocardiography showed that LV ejection fraction (LVEF) and LV fraction shortening (LVFS) gradually decreased with the prolongation of time after MI, suggesting a decline in LV systolic function, and only the MI + BF + BBIR-T group could delay the deterioration of cardiac function (Fig. 6e). On the 28th day after MI, the LV anterior wall (LVAW) of the MI + BF + BBIR-T group was thicker than the other groups in both the systolic and diastolic phases. At the same time, there was no significant difference in the LV posterior wall (LVPW) (Supplementary Fig. 8a). The LV volume was smaller in the MI + BF + BBIR-T group than in the other groups, suggesting that the BBIR-T cell therapy delayed cardiac deterioration primarily by delaying ventricular remodeling. The results of LV catheterization further confirmed the conclusions of echocardiography (Fig. 6f). Compared with the sham group, after 28 days of MI, the left ventricular pressure (LVP) and LV dP/dt maximum decreased, and the left ventricular end-diastolic pressure (LVEDP) and LV -dP/dt minimum increased, implying impaired LV systolic and diastolic function. Among the MI groups, the LVEDP and LV -dP/dt minimum in the MI + BF + BBIR-T group was lower than in other groups. At the same time, the LV dP/dt maximum was higher, indicating that the BBIR-T cell therapy not only delayed the deterioration of LV systolic function but also improved LV diastolic function.

The BBIR-T cell therapy could inhibit fibrosis expansion and improve cardiac remodeling but not aggravate inflammation response and tissue damage

Flow cytometry of cardiac pdgfrα-positive fibroblasts in the infarct and peri-infarct zone showed that only combined pre-labelled target cells and infusion of BBIR-T cells could clear F-Act. In contrast, unlabelled target cells or infusion of other effector cells had no significant effect on the number of the CD248-positive cells (Fig. 7a), further demonstrating the specificity of the BBIR-T cell therapy. IF staining also confirmed that only the MI + BF + BBIR-T cell group exhibited a significant reduction in CD248-positive cells in the peri-infarct zone (Supplementary Fig. 8b). The effect of clearance of F-Act on ventricular remodeling and cardiac fibrosis was evaluated by pathological analysis (Fig. 7b). Hematoxylin-eosin (HE) staining and Sirius red staining of the mouse hearts on the 28th day post-MI showed that the left ventricle had been severely remodelled, the ventricular wall was thinned, and the heart was enlarged. The thickness of the infarcted ventricular wall in the MI + BF + BBIR-T group was significantly thicker than in the other MI groups. The infarct zone (IZ) in the pathology was defined as the area of ventricular wall thinning. The peri-infarct zone (PIZ) was the area around the infarct zone that remained fibrotic, which was calculated by total fibrotic area minus the IZ area (Supplementary Fig. 7d).[26] Semi-quantifying the ratio of IZ size and the PIZ size to the LV area found that the BBIR-T cell therapy could not only reduce the infarct size but also inhibit the expansion of the peri-infarct zone. The pathological results showed that targeted clearance of F-Act could effectively inhibit fibrosis expansion and ventricular remodeling.

Brain natriuretic peptide (BNP) is mainly synthesized and secreted by ventricular myocytes. It reflects the compensatory function of the heart, and its level is proportional to the degree of heart failure[27]. Serum BNP level on the 28th day post-MI was detected by ELISA (Fig. 7c), which in the MI + BF + BBIR-T group was lower than other MI groups. Cardiomyocyte hypertrophy and pulmonary edema are important pathologic manifestations of ventricular remodeling. We measured the ratio of heart weight (HW) to body weight (BW) ratio, HW to tibia length (TL) ratio, and lung wet weight to dry weight ratio (Wet/Dry) (Fig. 7d-f) and found that the BBIR-T cell therapy could mitigate cardiomyocyte hypertrophy and pulmonary edema. In the undamaged myocardium of the remote zone, wheat germ agglutinin (WGA) staining, which labels cardiomyocyte membranes, showed that the cross-sectional area (CSA) of cardiomyocytes in the MI + BF + BBIR-T group was smaller than that of other MI groups. All these results further demonstrated that the BBIR-T cell therapy effectively alleviated the extent of heart failure.

In vivo, activation of traditional CAR-T cells leads to the sustained release of a large number of cytokines, known as cytokine release syndrome (CRS)[28], which increases the risk of myocarditis. In comparison, activation of BBIR-T cells is limited by the number of small molecules BF and does not activate indefinitely. Using Luminex X200 to detect the level of inflammatory cytokines in mouse myocardial tissue and peripheral blood 24 h after injecting effector cells (Fig. 8a, b), it was found that the BBIR-T cell therapy did not aggravate the release of

https://doi.org/10.1038/s41467-025-56703-2

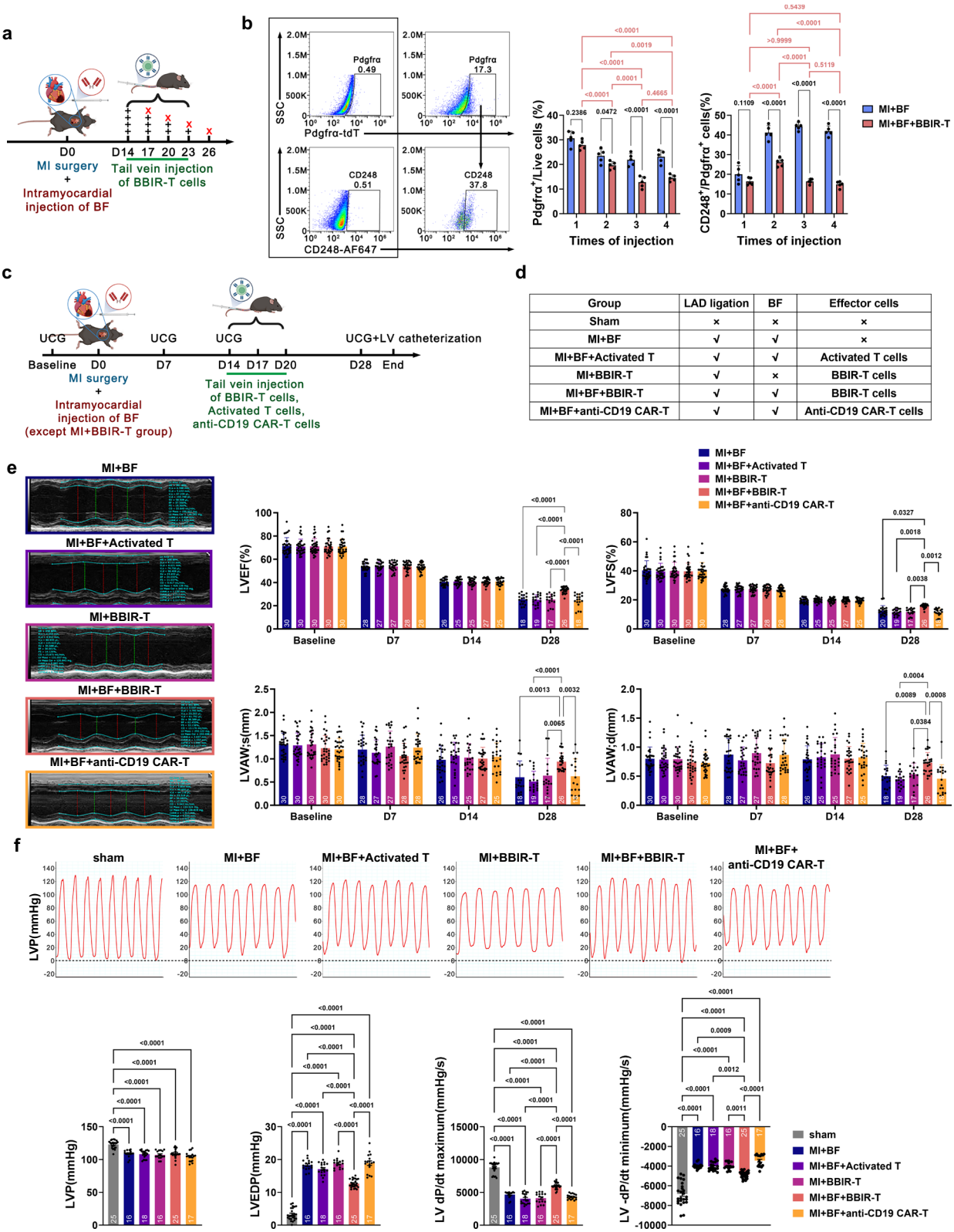

Group	LAD ligation	BF	Effector cells
Sham	×	×	×
MI+BF	√	√	×
MI+BF+Activated T	√	√	Activated T cells
MI+BBIR-T	√	×	BBIR-T cells
MI+BF+BBIR-T	√	√	BBIR-T cells
MI+BF+anti-CD19 CAR-T	√	√	Anti-CD19 CAR-T cells

inflammatory cytokines. HE staining of the liver, spleen, lung, and kidney showed no significant tissue damage, reflecting that the BBIR-T cell therapy did not cause damage to the off-target organs (Fig. 8c). The above results demonstrated the safety of the BBIR-T cell therapy.

To clarify the long-term effects of the BBIR-T cell strategy, we conducted a three-month observation on different treatment groups. As shown in Supplementary Figs. 9b-e, the cardiac function of mice were evaluated using echocardiography and LV catheterization. Comparing to the cardiac function one month after MI (Fig. 6e-f), the mice showed a continuous decline in both systolic and diastolic functions over the course of three months. However, the MI + BF + BBIR-T group retained a relative advantage, with statistically significant improvements in cardiac systolic and diastolic functions compared to other groups. This suggests that BBIR-T cell therapy can delay the deterioration of cardiac function in mice for at least three months following MI. Histopathological examination revealed no significant

Fig. 6 | Three-time injections of BBIR-T cells improved the cardiac function of MI mice. a Schematic diagram of the number of BBIR-T-cell injections. Pdgfra-CRE:tdTomato mice were intramyocardially injected with biotinylated anti-CD248 F(ab')2 immediately after MI surgery to label the F-Act. A total of 10^6 BBIR-T cells were injected into the tail vein every three days beginning 14 days after MI. Mouse hearts were obtained for flow cytometry detection three days after BBIR-T cells injection. Created in BioRender. Haiting, C. (2025) https://BioRender.com/m61n139. **b** Flow cytometry of fibroblasts isolated from hearts of C57BL/6J WT and Pdgfra-CRE:tdTomato mice. Total cardiac fibroblasts were lineage traced by pdgfrα. F-Act was marked with antibodies against CD248-AF647. Quantifying the pdgfrα$^+$ fibroblast ratio in live cells and the CD248$^+$ cell ratio in pdgfrα$^+$ fibroblasts. $n = 5$ mice at each group. Data are mean ± SEM and p-values are displayed in the bar charts, two-way ANOVA followed by Šídák multiple comparison test, one-way ANOVA followed by Tukey's multiple comparison test. **c, d** Schematic diagram of the animal experiments. Mice were divided into 6 groups: sham, MI + BF, MI + BF + Activated T, MI + BBIR-T, MI + BF + BBIR-T, and MI + BF + anti-CD19 CAR-T. Each group underwent echocardiographic detection before, at 7, 14, and 28 days after MI surgery. The sham group only underwent chest opening without ligating the LAD; the remaining 5 groups underwent LAD ligation. Except for the sham and MI + BBIR groups, the other groups were injected intramyocardially with BF immediately after MI. On the 14th, 17th, and 20th days post-MI, except for the sham and MI + BBIR groups, the other groups were injected intravenously with different effector cells. All mice were tested for LV catheterization 28 days after MI and sacrificed for subsequent experiments. Created in BioRender. Haiting, C. (2025) https://BioRender.com/y36t712. **e** Typical short-axis M-type echocardiographic images in each group of mice 28 days after MI. The LVEF, LVFS, and LVAW thickness were quantified at different time points. The number of surviving mice (n) for each treatment group at each time point was displayed at the bottom of the bar chart. Data are mean ± SEM and p-values less than 0.05 are displayed in the bar chars, two-way ANOVA followed by Tukey's multiple comparisons tests. **f** Typical LVP image of each group of mice detected by LV catheterization. The LVP, LVEDP, LV dP/dt maximum, and LV -dP/dt minimum were quantified. The number of mice (n) for each treatment group was displayed at the bottom of the bar chart. Data are mean ± SEM and p-values are displayed in the bar charts, one-way ANOVA followed by Tukey's multiple comparison test. Source data are provided as a Source Data file.

differences in LV wall thickness and fibrosis among the different treatment groups (Supplementary Fig. 9f). These results suggested that a single F-Act removal was insufficient to sustain anti-fibrotic effect over the long term. Due to the continued presence of pathological triggers, F-act will continue to differentiate and activate. Multiple treatments targeting F-act may achieve more favorable outcomes.

Together, the BBIR-T cell therapy could effectively clear CD248-positive F-Act. Moreover, the clearance of F-Act after scar maturation could significantly inhibit fibrosis expansion and cardiomyocyte hypertrophy, thereby improving ventricular remodeling and delaying the deterioration of cardiac function.

Discussion

Our work observed that the pathogenic fibroblast subpopulation F-Act is a critical cause of tissue repair disorders following MI. Continuous activation of F-Act during the mature phase of post-MI repair leads to fibrosis expansion and adverse ventricular remodeling, ultimately leading to heart failure. To precisely remove abnormally activated F-Act cells from the heart, we developed a bio-controllable BBIR-T cell therapy based on identifying the F-Act characteristic surface antigen CD248. This therapy effectively inhibits fibrosis expansion and cardiomyocyte hypertrophy in the peri-infarct zone, thereby improving ventricular remodeling and delaying the deterioration of cardiac function.

Cardiac fibrosis after MI is an important process of tissue repair, but excessive fibrosis expansion after scar maturation leads to adverse ventricular remodeling and deterioration of cardiac function. The ventricular scar heterogeneity provides a substrate for reentrant circuits and thereby induces ventricular tachycardia[29]. Cohort studies based on cardiac magnetic resonance imaging have shown that MI patients with a larger PIZ still have a poor prognosis, even if the infarct size at the time of infarction was not large and the systolic function was not severely impaired[30]. Our study also confirms that inhibiting fibrosis expansion in the peri-infarct zone after scar maturation can significantly inhibit ventricular remodeling, which is clinically important for improving heart failure and preventing possible ventricular arrhythmias in the future.

The BBIR-T cell therapy has clear advantages compared with traditional CAR-T therapy in the condition of MI. First, not all fibroblasts after MI are harmful, and efforts to clear the pathogenic fibroblast subpopulation should be committed without damaging beneficial fibroblasts such as F-Myo and F-MFC. Two studies have applied CAR-T cells to remove cardiac fibroblasts with beneficial outcomes in improving cardiac function[6,21,31]. In both studies, cardiac fibrosis was induced by angiotensin II and phenylephrine, and FAP was selected as the target antigen for fibroblasts. However, FAP is widely expressed in cardiac fibroblasts, especially in F-Myo and F-MFC. Premature inhibition of fibrosis and overly widespread killing of fibroblasts via FAP would be detrimental to post-infarction repair and increase the risk of heart rupture. Therefore, the BBIR-T cell therapy abandoned previously reported non-specific fibroblast antigen and identified F-Act-specific target antigen—CD248, significantly reducing off-target effects on fibroblast subpopulations. Secondly, considering that CD248 is also expressed in small amounts in tissues and organs other than the heart, the BBIR-T system draws on the structure of universal CAR, designs the antigen-specific domain as a third-party small molecule, and limits the effect of BBIR-T cells into injured myocardium by intramyocardial injection of BF to reduce the off-target effect on other organs. Third, the activation of universal CAR-T cells is limited by the number of third-party molecules that would not be indefinitely activated, reducing the release of inflammatory cytokines and thereby reducing the occurrence of explosive myocarditis. Finally, the BBIR-T cell therapy is time-controllable. Controlling the timing of intravenous injection of BBIR-T cells after scar maturation minimizes the risk of poor scar formation and heart rupture.

The initially identified F-Act-specific antigen CD248 is a type I transmembrane protein mainly expressed in fibroblasts and has been experimentally shown to represent F-Act effectively. A distinctive characteristic of CD248 is its temporal expression pattern. CD248 functions during embryo development and is either not expressed or found at deficient levels in adult tissues[32]. Another advantage of CD248 as a target antigen is that its amino acid sequence is highly conserved between species. Alignment of the mouse and human amino acid sequences showed an overall 77.5% identity[24]. Therefore, CD248-specific CAR-T therapy can be optimally designed and applied to clinical practice.

In parallel with our work, Li G, et al. utilized single-cell and spatial molecular profiling of infarcted mouse hearts to identify a subset of cardiac fibroblasts expressing CD248, which plays a crucial role in long-term pathological remodeling and cardiac dysfunction[33]. Notably, these CD248$^+$ fibroblasts are spatially enriched in specific cardiac niches and exhibit strong interactions with cardiac T cells. Mechanistically, this interaction is mediated by CD248-dependent stabilization of ACKR3 through TGF-βRI, ultimately promoting T cell adhesion and retention. Disruption of this interaction using monoclonal antibodies or anti-CD248 CAR-T cells leads to reduced cardiac fibrosis and improved cardiac function. Importantly, their findings align closely with our results, further supporting the critical role of CD248$^+$ fibroblasts in cardiac fibrosis and highlighting the therapeutic potential of targeting this fibroblast-immune interaction.

In the scRNA-seq of this study, CD248 was also highly expressed in the F-SH subpopulation with high expression of the progenitor cell/

https://doi.org/10.1038/s41467-025-56703-2

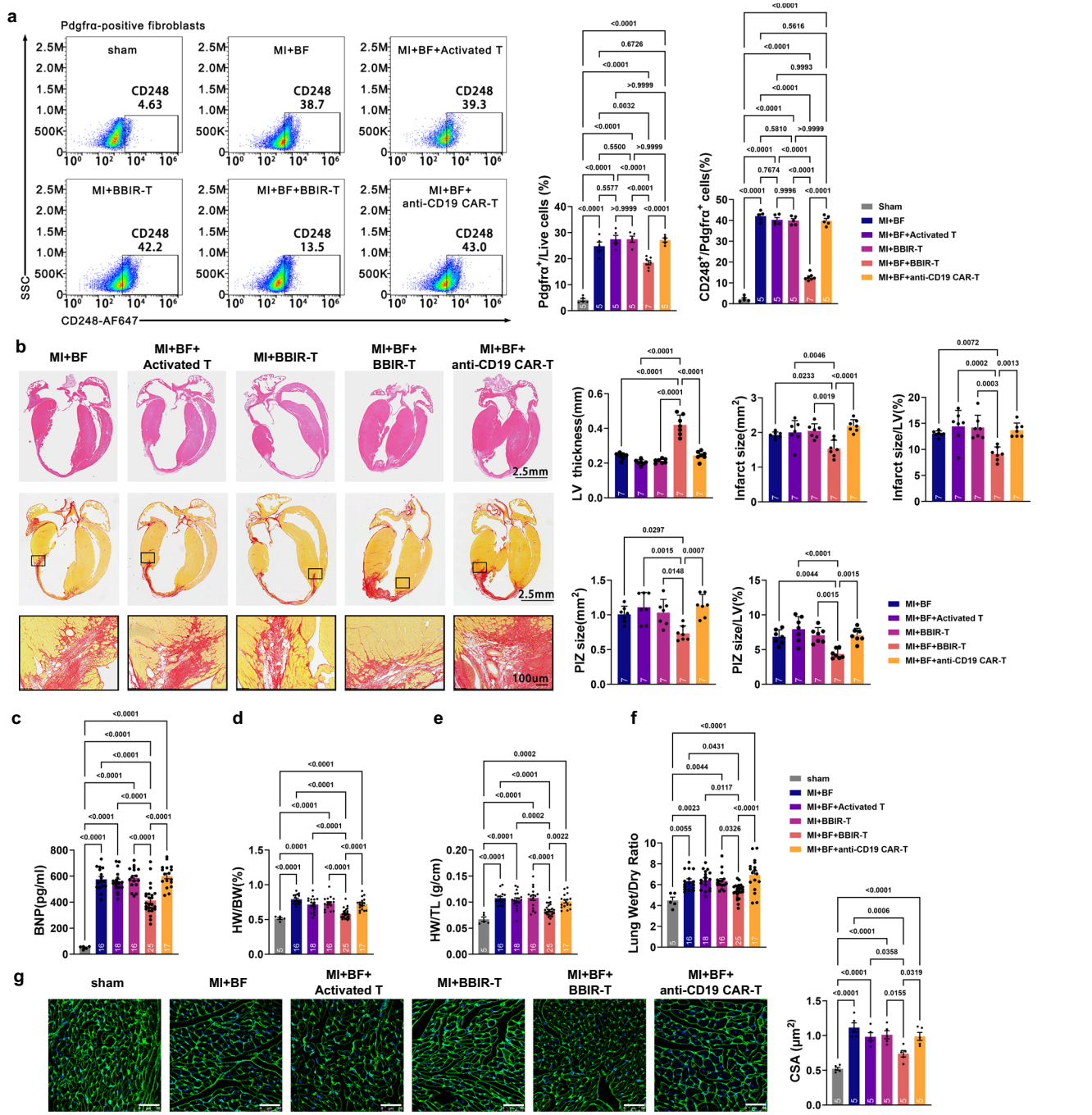

Fig. 7 | The BBIR-T cell therapy could inhibit fibrosis expansion and improve cardiac remodeling. a Flow cytometry of fibroblasts isolated from hearts of C57BL/6 J WT and Pdgfra-CRE:tdTomato mouses. Typical images show CD248$^+$ F-Act versus the pdgfrα$^+$ fibroblasts ratio. Quantifying the pdgfrα$^+$ fibroblast ratio in live cells and the CD248$^+$ F-Act ratio in pdgfrα$^+$ fibroblasts. $n = 7$ mice in the MI + BF + BBIR-T group and $n = 5$ mice in other groups. **b** Representative full-view images of heart HE and Picro-Sirius Red staining, magnifying the PIZ. Scale bars = 2.5 mm and 100 μm. Quantifying LV wall thickness (mm), infarct size (mm^2) and PIZ size (mm^2). Calculating the ratio of infarct size or PIZ size to LV area. $n = 7$ mice of each group. **c** Serum BNP levels were detected by ELISA. The number of mice (n) in each group was labelled in the bottom of the bar chart. **d**–**f** HW/BW ratio, HW/TL ratio and lung wet/dry weight ratio were shown. The number of mice in each group was labelled in the bottom of the bar charts. **g** Double staining of fluorescent WGA-FITC and DAPI. Scale bar = 50 μm. Quantify each group's cardiomyocyte CSA (μm^2). $n = 5$ mice of each group. **a**–**g** Data are mean ± SEM and p-values are displayed in the bar charts, one-way ANOVA followed by Tukey's multiple comparison test. Source data are provided as a Source Data file.

stem cell marker *Sca1*, which is consistent with the expression of CD248 in mesenchymal stem cells reported in other studies[24]. Despite the low proportion of Sca1$^+$ progenitor-like fibroblasts in the adult cardiac interstitium[34], pseudotime trajectory analysis showed that F-SH and F-Act were in the same branch, suggesting that F-SH has the potential to differentiate into F-Act during post-MI injury and repair[10]. Consequently, the cardioprotective effects observed with the CD248-targeted BBIR-T cell therapy may, at least in part, be attributed to the removal of F-SH cells.

The long-term efficacy analysis revealed that the beneficial effects of BBIR-T cell therapy in anti-fibrosis and anti-ventricular remodeling were weakened in mice 3 months post-MI, compared to 1 month post-MI. Consequently, if long-term efficacy is desired, redosing of BBIR-T cells is necessary. Given that the depletion of biotinylated antibodies

https://doi.org/10.1038/s41467-025-56703-2

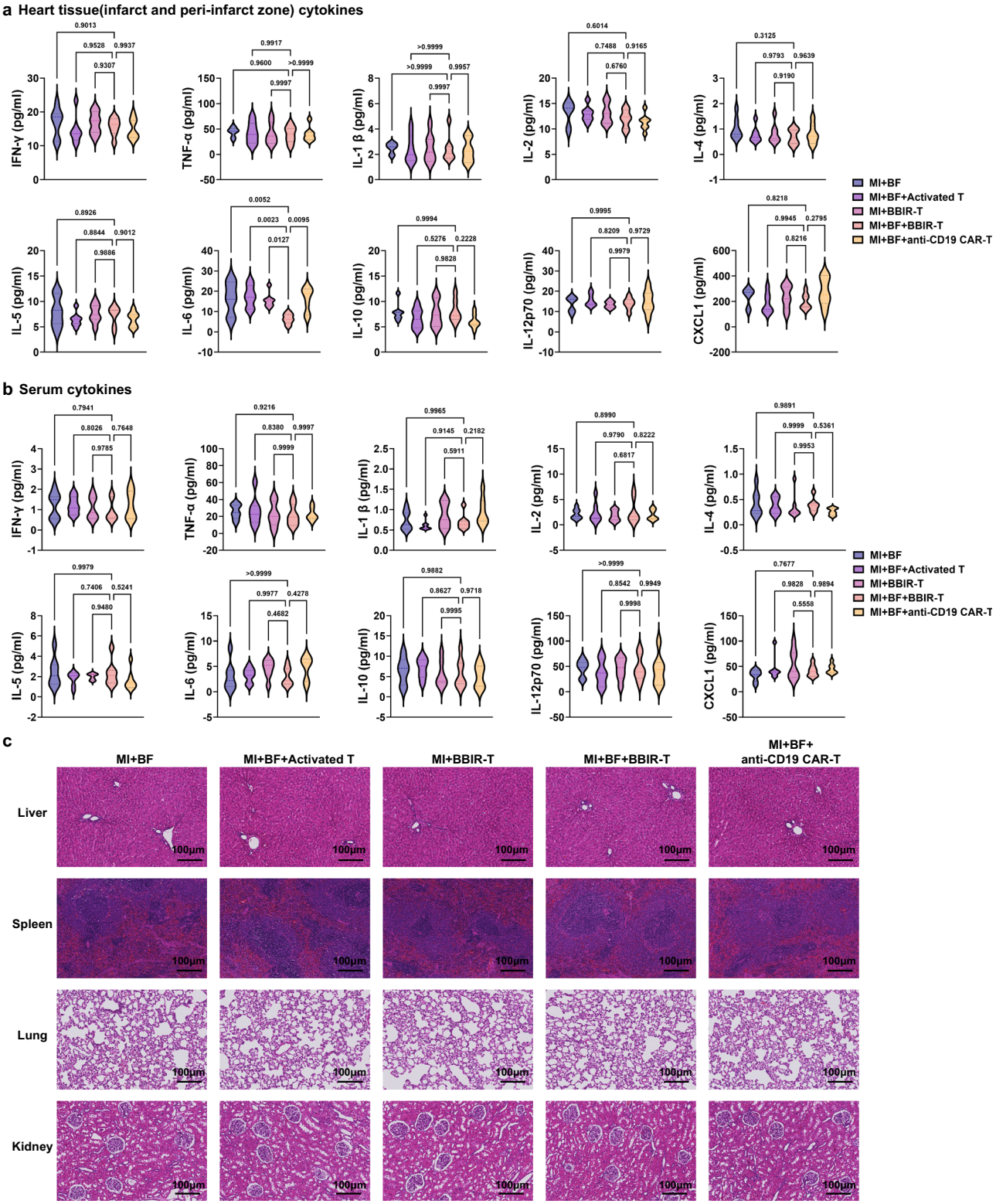

Fig. 8 | The BBIR-T cell therapy did not aggravate inflammation response and tissue damage. Luminex assay was performed using the Bio-Plex 200 system with standard controls to detect the concentrations of IFN-γ, TNF-α, IL-1β, IL-2, IL-4, IL-5, IL-6, IL-10, IL12p7, and CXCL1 in heart tissue lysates (**a**) and serum (**b**). $n = 6$ mice of each group. *P*-values are displayed in the violin plots, one-way ANOVA followed with Dunnett's comparison test. **c** Representative images of HE staining of the liver, spleen, lung, and kidney. Scale bar = 100 μm. Each experiment was repeated 5 times independently with similar results. Source data are provided as a Source Data file.

prevents the activation of BBIR-T cells, in mice, we can re-inject biotinylated anti-CD248 F(ab')2 intramyocardially to target and mark the CD248 positive cells. In humans, this can be achieved through intracoronary administration. Therefore, re-administering BBIR-T cell therapy after one month is feasible and may enhance the long-term translational potential of this therapy.

This study found that clearance of CD248-positive F-Act cells after scar maturation could inhibit fibrosis and improve cardiac function,

confirming the pathogenic role of the F-Act subpopulation in tissue repair disorders after MI. However, F-Act's source, proliferation, activation mechanism and the downstream signaling pathways that promote fibrosis still need further study. Although the BBIR-T cell therapy did not exacerbate myocardial inflammation or off-target tissue damage in this study, CAR-T therapy is still immature. It is necessary to explore safer and more effective targets for inhibiting F-Act cell activation and proliferation.

Methods

Ethics declarations

All procedures involving animals were approved by the Institution Ethics Committee of Anhui Medical University (Anhui, China) (No. LLSC20230846) and performed in accordance with the guidelines from Directive 2010/63/EU of the European Parliament. All experiments involving human specimens were approved by the research ethics committees of the First Affiliated Hospital of Zhejiang University (Zhejiang, China). All procedures had local ethical approval, and all experiments were conducted according to the 2013 Declaration of Helsinki.

Human specimens

The human infarcted heart sample was collected from a 53-year-old female who was diagnosed with MI before heart transplantation. The sample was taken from the left ventricle during the surgery. Written informed consent was obtained from the patient. The sample was collected from the First Affiliated Hospital of Zhejiang University in September 2019. The baseline characteristics of the patient are summarized in Supplementary Data 1.

Animals

The mouse lines used in this study were as follows. C57BL/6J mice (No. N000013) were purchased from Gempharmatech Co., Ltd. Pdgfra-CRE:tdTomato mice were obtained by crossing Pdgfra-CRE mice from Shanghai Biomodel Organism CO., Ltd (JAX: 013148) and Rosa26-CAG-LSL-Cas9-tdTomato mice from Gempharmatech Co., Ltd (No. T002249). Genotyping was conducted using a Mouse Direct PCR kit (Bimake, B40015). Mice 8-10 weeks old were randomly assigned to different experimental groups. Animals were fed a standard laboratory diet with free access to chow and water. The feeding environment temperature was 22 ± 1 °C, and the humidity was 65-70%, with a 12-hour light-dark cycle.

Cell lines and cell culture

NIH-3T3 (BC-C-MI-015) and HEK-293T (BC-C-HU-044) cells were purchased from Nanjing BioChannel Biotechnology Co., Ltd. The cell lines were authenticated and maintained by the supplier and no additional authentication was performed. The cell lines were confirmed to be mycoplasm-free with a mycoplasma detection kit and treated with mycoplasma elimination reagent (BioChannel, BC-CE-019) for prevention of mycoplasma contamination. The cell lines were cultured in DMEM (BioChannel, BC-M-033, with 4.5 g/L glucose, 0.584 g/L L-glutamine). The culture medium was supplemented with 10% Foetal Bovine Serum (BioChannel, BC-SE-FBS01), penicillin and streptomycin (BioChannel, BC-CE-007). Cells were maintained at 37°C in an atmosphere of humidified air containing 5% CO_2. Cells were routinely passaged every 2-3 days and not allowed to grow to confluence.

The cell line NIH-3T3 was used for the preparation of target cells. NIH-3T3 were transduced with *Cd248* overexpression (OE) and knockout (KO) lentiviruses (GeneChem, 69129-2 and 10613-1) to obtain *Cd248*-OE and *Cd248*-KO NIH-3T3 cells.

Primary T cells extraction and culture

Human T cells were derived from the peripheral blood of healthy donors, and mouse T cells were derived from the spleen of 4-week-old healthy C57BL/6 J mice. Human PBMCs and mouse splenic lymphocytes were isolated using lymphocyte separation medium (TBD Science, LTS1077 and LTS1092PK) gradient centrifugation and seeded in culture plates precoated with anti-CD3 antibody (1 μg/mL, Invitrogen, 14-0037-82 and 16-0031-85) and anti-CD28 antibody (1 μg/mL, Invitrogen, 16-0289-85 and 16-0281-85). The cells were cultured in RPMI 1640 (BioChannel, BC-M-017, with 2 g/L glucose, 0.3 g/L L-glutamine). Culture medium was supplemented with 10% Foetal Bovine Serum (BioChannel, BC-SE-FBS01), penicillin and streptomycin (BioChannel, BC-CE-007), IL-2 (20 ng/mL, Peprotech, 200-02 and 212-12), IL-7 (10 ng/mL, Peprotech, 200-07 and 217-17), and IL-15 (10 ng/mL, Peprotech, 200-15 and 215-15). Cells were maintained at 37°C in an atmosphere of humidified air containing 5% CO_2.

Preparation of BBIR-T cell system

The BBIR-T cell system consisted of dcAv-expressed BBIR-T cells and the antigen-specific molecular BF. The BBIR-T cells and anti-CD19 CAR-T cells were obtained by transducing primary T cells using lentivirus LV-dcAv.BBIR and LV-anti-CD19.CAR. Ten milligrams of anti-CD248 monoclonal antibody (Promab, 31613) were digested by pepsin and purified by ultrafiltration or molecular sieve to obtain anti-CD248 F(ab')2, followed by labelling with a biotinylation kit (Thermo Fisher Scientific, 21435).

Surgically induced mouse acute MI model

Mice 8-10 weeks old were anesthetized with 1-1.5% isoflurane, and body temperature was maintained at 37°C using a feedback-controlled heating pad throughout the surgery. All surgical instruments were sterilized before the surgery. Hair was removed from the surgical site and disinfected with iodophor. Mice were ventilated with a rodent ventilator after endotracheal intubation. Hearts were exposed via the fourth left intercostal incision, followed by ligation of the left anterior descending coronary artery. Sham-operated mice underwent surgical incisions without ligation.

Left ventricular catheterization

Invasive hemodynamics were assessed by LV catheterization performed 4 weeks post-MI. A Millar Mikro-Tip 1.4 F pressure transducer (Millar Instruments, SPR-839) was introduced into the left ventricle via the right carotid artery under pentobarbital sodium (30 mg/kg) anesthesia. Ventricular pressure was recorded by a PowerLab multi-channel physiological recorder (PowerLab35). LVP (mmHg), LVEDP (mmHg), LV +dP/dt maximum (mmHg/s), and LV -dP/dt minimum (mmHg/s) were analyzed using Labchart v8.1.5 software.

Echocardiography

Mouse cardiac function was assessed blinded to grouping information using Vevo 2100 transthoracic echocardiography (Visualsoics) before and 7, 14, and 28 days after MI surgery. After induction of anesthesia with isoflurane, hearts were imaged in two-dimensional and M-mode. Two-dimensional short and long axes were visualized. Three representative cycles were captured for each animal at each time point, and measurements for the left ventricular anterior wall thickness (LVAW;s, μm, and LVAW;d, μm) and left ventricular posterior wall thickness (LVPW;s, μm, and LVPW;d, μm) were obtained and averaged. Left ventricular volume (LV vol;s, mm^2, and LV vol;d, mm^2), left ventricular ejection fraction (LVEF, %), and left ventricular fractional shortening (LVFS, %) were calculated automatically.

Single-cell dissociation and cell sorting

Single-cell samples were derived from the hearts of mice in three groups: sham group, 7 days post-MI, and 14 days post-MI. Each group consisted of 2 samples, with interstitial cells from the hearts of 3 mice collected in each sample. A similar protocol was followed as previously described after collecting the mouse hearts to obtain single cells.

Briefly, the left ventricles were first washed with PBS, minced into small pieces (approximately 1 mm^3) on ice, and enzymatically digested in the DMEM + 0.5 mg/mL Liberase medium (Roche) for 20–30 min at 37 °C. After digestion, the samples were sieved through a 40-μm cell strainer and centrifuged at 300 *g* for 5 min. After the supernatant was removed, noncardiomyocyte sample pelleted cells were suspended in red blood cell lysis buffer (Miltenyi Biotec) to lyse the red blood cells. The single-cell suspension was further enriched using a MACS Dead Cell Removal Kit (Miltenyi Biotec). The enriched single cells were then stained with 7-AAD Viability Staining Solution (FcmacsBiotech) for viability assessment. Subsequently, the cell pellet was suspended in relevant solutions for further experiments.

Processing of scRNA-seq data

We performed scRNA-seq of six pooled samples from 0, 7, and 14 days after MI surgery separately. Raw scRNA-seq data were processed using 10× Genomics Cell Ranger software (version 3.1.0). Analyses of scRNA-seq data were analyzed in R version 4.0 using Seurat suite version 3.2.3. For the initial quality control filtering, we excluded low-quality cells (<400 genes/cell, >20000 genes/cell, and 10% mitochondrial transcript presence/cell). Then, we used Seurat v3 with default parameters to integrate the datasets collected from different samples and remove the batch effect. Dimensionality reduction using PCA was undertaken to explore the heterogeneity. UMAP was used for reduction to two dimensions for visualization purposes. Markers for a specific cluster were found with the function FindAllMarkers (min.pct=0.25, logfc.threshold=0.25).

Stereo-seq preparation and sequencing

Tissue collection and processing. Heart samples were obtained from two sham and two MI hearts of C57BL/6 J mice. These tissues were collected 10 days post-sham/MI surgery, promptly embedded in pre-cooled Tissue-Tek OCT (Sakura, 4583), and snap-frozen in prechilled isopentane with liquid nitrogen until the OCT solidified. The embedded tissues were then sectioned to a thickness of 10 μm using a Leica CM1950 cryostat, and either mounted on glass slides for Nissl staining or placed on pre-chilled Stereo-seq capture chips for subsequent Stereo-seq procedures. The Stereo-seq protocol was conducted as previously outlined[35]. Initially, the Stereo-seq capture chips underwent washing with NF-H2O containing 0.05U/μL RNase inhibitor (NEB, M0314L) and were air-dried at room temperature. Cryosections were then affixed to the chips' surfaces and incubated at 37 °C for 5 min. Following this, the chips with sections were subjected to fixation in pre-cooled methanol at −20 °C for 40 min.

In situ reverse transcription. Post-fixation, the chips bearing tissues were removed, air-dried, and subsequently washed with a wash buffer composed of 0.1X SSC buffer (Thermo, AM 9770) enriched with 0.05U/μL RNase inhibitor (NEB, M0314L). The tissue sections on the chips were permeabilized using 0.1% pepsin (Sigma, P7000) in 0.01 M HCl buffer, followed by a 6-minute incubation at 37 °C. The permeabilization agent was then discarded, and the chips were rewashed with the wash buffer. RNA liberated from the permeabilized tissues and captured by the DNB underwent reverse transcription at 42 °C for 2 h using SuperScript II (Invitrogen, 18064-014), which included 10 U/μl reverse transcriptase, 1 mM dNTPs, 1 M betaine solution PCR reagent, 7.5 mM MgCl2, 5 mM DTT, 2 U/μl RNase inhibitor, and 2.5 μM Stereo-seq-TSO [5-CTGCTGACGTACTGAGAGGC/rG//rG//iXNA_G/ − 3] in 1× First-Strand buffer. The tissues were subsequently washed twice with the wash buffer and extracted from the chips using a tissue removal buffer (10 mM Tris-HCl, 25 mM EDTA, 100 mM NaCl, and 0.5% SDS) at 37 °C for 30 min. The chips were then treated with Exonuclease I (NEB, M0293L) at 37 °C for 1 h and washed twice with the wash buffer. The resultant first strand cDNAs on the chips were amplified using KAPA HiFi Hotstart Ready Mix (Roche, KK2602) with a 0.8 μM cDNA-PCR primer (5-CTGCTGACGTACTGAGAGGC-3), followed by a 5-minute incubation at 95 °C, 15 cycles of 98 °C for 20 sec, 58 °C for 20 sec, and 72 °C for 3 min, concluding with a final incubation at 72 °C for 5 min.

Library construction and sequencing. The concentrations of the purified cDNA products were assessed using the Qubit™ dsDNA Assay Kit (Thermo, Q32854). A total of 20 ng of these products were fragmented using in-house Tn5 transposase at 55 °C for 10 min, with the reaction halted by the addition of 0.02% SDS. The fragmented products were subsequently amplified as follows: 25 μl of the fragmentation product, 1× KAPA HiFi Hotstart Ready Mix, 0.3 μM Stereo-seq-Library-F primer (/5phos/CTGCTGACGTACTGAGAGG*C*A-3), and 0.3 μM Stereo-seq-Library-R primer (5-GAGACGTTCTCGACTCAG-CAGA-3) in a total volume of 100 μl, supplemented with nuclease-free H2O. The amplification protocol consisted of a 5-minute initial cycle at 95 °C, 13 cycles of 98 °C for 20 sec, 58 °C for 20 sec, and 72 °C for 30 sec, and a final cycle at 72 °C for 5 min. The PCR products were then purified using VAHTS DNA Clean Beads (0.6× and 0.15×). The final library was utilized for DNB generation and sequenced on the MGI DNBSEQ-Tx sequencer at China National Gene Bank (CNGB), with read 1 at 35 bp and read 2 at 100 bp.

Spatial reconstruction of scRNA-seq Data. To investigate the spatial distribution of fibroblast subpopulations from scRNA-seq data based on spatial transcriptome data, we first defined marker gene sets for each fibroblast subtype: F-Act and F-Myo. The top 10 marker genes for each subpopulation were selected based on their adjusted *p*-values and log fold changes, ensuring that there was nearly no overlap between the marker sets, thus confirming the uniqueness of these cell populations. The spatial distribution of fibroblast subpopulations was then calculated using the 'AddModuleScore' function in Seurat[20]. This function computes a module score[36] for each spot in the spatial transcriptome data based on the average expression levels of the marker gene sets. The spatial organization and heterogeneity of F-Act and F-Myo were visualized using the "SpatialFeaturePlot" function in Seurat, which maps the identified fibroblast subtypes onto the tissue sections.

Cytokine/chemokine assay

For cytokine/chemokine quantification, serum samples were obtained as described for ELISA, and heart tissue lysate samples were obtained by lysis buffer for multicytokines (Absin, abs9225) supplemented with a general protease inhibitor cocktail (Absin, abs9161). IL-1β, IL-2, IL-4, IL-5, IL-6, IL-10, TNF-α, IFN-γ, IL-12p70, and CXCL1 concentrations were measured in tissue lysates and cell culture supernatants using a Bio-Plex Pro Cytokine Panel (Bio-Rad) according to the manufacturer's instructions. Data were collected using the Luminex X200 (Luminex xMAP) and analyzed by the software Milliplex Analyst Version 5.1.

Immunofluorescence

Mouse tissue samples were fixed in 4% PFA for 2-3 h and then dehydrated overnight in 30% sucrose solution, followed by OCT (Tissue Tek) embedding and preparation of 5 μm cryosections. Cryosections were blocked with 10% goat serum for 1 h at room temperature, followed by overnight primary antibody incubation at 4 °C. After rinsing 3 times in PBS, sections were incubated with secondary antibody and DAPI for 2 h at room temperature. A confocal laser microscope (Leica) was used to acquire staining images, and semi-quantitative immunofluorescence analysis was performed with Image-Pro Plus software. Primary antibodies were Periostin (1:200, Abcam, ab14041), αSMA (1:200, Cell Signaling, 19245 and 48938), CD248 (1:1000, Santa Cruz, sc-377221), COMP (1:1000, Genetex, GTX14515), CD31 (1:200, BD Biosciences, 550300), Ly6G (1:200, Abcam, ab25377), CD68 (1:200, Abcam, ab955), and CD11b (1:200, BD Biosciences, 550282). The secondary antibodies used in this study included goat anti-mouse IgG (1:1000, Invitrogen, A10521 for

cyanine3), goat anti-rabbit IgG (1:1000, Invitrogen, A11008 for Alexa Fluor 488), and goat anti-mouse F(ab) (1:200, Abcam, ab98757 for DyLight 488).

Flow cytometry

Isolation of cells from freshly collected cardiac tissue was performed by cutting the heart into pieces, followed by digestion in Liberase (Roche) at 37 °C for 15 min. All prepared cells were suspended in staining buffer (BD Biosciences) and then incubated with antibodies conjugated to cell surface markers for 30 min. The stained cells were incubated in fixation/permeabilization solution (BD Biosciences) for 15 min before incubation with antibodies conjugated to cytoplasmic markers for 30 min. After incubation with or without fluorescent secondary antibodies, the cells were analyzed using a BD FACS Aria II or C6 flow cytometer (BD Biosciences). The antibodies used in this study included Periostin (Abcam, ab14041), αSMA-Alexa Fluor 647 (Novus, NBP2-34522), CD248-Alexa Fluor 647 (Santa Cruz, sc-377221), CD3-FITC (BioLegend, 317306 for human and 100204 for mouse), CD4-APC (BioLegend, 344614 for human and 100412 for mouse), CD8-PE (BioLegend, 344706 for human and 100708 for mouse), and goat anti-rabbit IgG (1:1000, Invitrogen, A11008 for Alexa Fluor 488).

Western blotting

Cells or heart tissue were lysed in RIPA lysis buffer supplemented with phosphatase inhibitor tablets (Roche) and protease inhibitor tablets (Roche). Protein concentrations were determined by BCA assay (Thermo Fisher Scientific). Samples were loaded on 4-12% Bis-Tris SDS-PAGE gels (Invitrogen) and transferred onto PVDF membranes (Millipore). Membranes were blocked with 5% BSA in TBST and incubated against the primary antibodies. GAPDH was used as a loading control. Detection was carried out using HRP-conjugated corresponding secondary antibodies. Protein bands were visualized using enhanced chemiluminescence (Thermo Fisher Scientific). Primary antibodies were CD248 (1:1000, Santa Cruz, sc-377221) and CD3ζ (1:1000, Abcam, ab243874), and accordingly, secondary antibodies were HRP-conjugated goat anti-mouse IgG (1:4000, Proteintech, SA00001-1) and HRP-conjugated goat anti-rabbit IgG (1:4000, Proteintech, SA00001-2).

Cytotoxicity assay

To detect the killing effect of effector cells on the target cell and determine the optimal E:T ratio, target cells were cocultured for 24 h with effector cells at different E:T ratios, from 2 to 20. To verify the safety of the BBIR-T therapy in vitro, target cells were cocultured for 24 h with different effector cells, including active T cells, BBIR-T cells, and anti-CD19 CAR-T cells. Cytotoxicity was detected by CCK-8 (Vazyme, A311-01) and LDH Cytotoxicity Assay Kit (Beyotime, C0017).

Enzyme-linked immunosorbent assay (ELISA)

Cytokines IL-2 and IFN-γ in cell coculture supernatants were detected using the corresponding human ELISA kits according to the manufacturer's instructions (Multi-Science, EK102, EK180). Blood samples were centrifuged to collect serum. BNP levels in serum were measured using a commercial ELISA kit (Elabscience, E-EL-M0204c) according to the protocol provided.

Histopathology

HE staining, Picrosirius Red staining and WGA staining were performed 4 weeks post-MI. Hearts were arrested in diastole following intraventricular injection of 10% potassium chloride (KCl) and then excised and washed in PBS. Tissues were fixed with 4% phosphate-buffered formalin (pH 7.4), gradually dehydrated, embedded in paraffin, and cut into transverse sections (5 μm thickness). HE staining, picrosirius red staining, and WGA staining were performed according to the manufacturer's instructions. The images were acquired using a Leica SCN400 slide scanner (Leica).

Statistical analysis

GraphPad Prism 9.0 was used to draw statistical images and perform comparative analyses. The data were presented as the mean ± SEM. Data were tested using either two-tailed, unpaired Student's *t*-test or one-way analysis of variance (ANOVA) followed by Tukey's multiple comparisons tests to determine differences between groups at a single time point. Data were tested using two-way ANOVA followed by Bonferroni's multiple comparisons tests to determine differences between groups at multiple time points. $P < 0.05$ was considered to be statistically significant.

Reporting summary

Further information on research design is available in the Nature Portfolio Reporting Summary linked to this article.

Data availability

The raw scRNA-seq data reported in this study have been deposited in the Genome Sequence Archive in the National Genomics Data Cente, Beijing Institute of Genomics (China National Center for Bioinformation), and Chinese Academy of Sciences, under accession numbers CRA005739 and HRA001765, respectively, and are publicly accessible at https://ngdc.cncb.ac.cn. The public data on membrane proteins used in this study can be viewed in HPA (https://www.proteinatlas.org/). All the other data supporting the findings of this study are available in the article and its Supplementary Materials and from the corresponding authors upon reasonable request. Source data are provided with this paper.

Code availability

The code and R scripts related to the findings of this study are available upon reasonable request.

References

1. Bhatt, D. L., Lopes, R. D. & Harrington, R. A. Diagnosis and Treatment of Acute Coronary Syndromes: A Review. *JAMA* **327**, 662–675 (2022).
2. Frantz, S., Hundertmark, M. J., Schulz-Menger, J., Bengel, F. M. & Bauersachs, J. Left ventricular remodelling post-myocardial infarction: pathophysiology, imaging, and novel therapies. *Eur Heart J* **43**, 2549–2561 (2022).
3. Tallquist, M. D. & Molkentin, J. D. Redefining the identity of cardiac fibroblasts. *Nat Rev Cardiol* **14**, 484–491 (2017).
4. Forte, E. et al. Dynamic Interstitial Cell Response during Myocardial Infarction Predicts Resilience to Rupture in Genetically Diverse Mice. *Cell Rep* **30**, 3149–3163 e3146 (2020).
5. Kaur, H. et al. Targeted Ablation of Periostin-Expressing Activated Fibroblasts Prevents Adverse Cardiac Remodeling in Mice. *Circ Res* **118**, 1906–1917 (2016).
6. Aghajanian, H. et al. Targeting cardiac fibrosis with engineered T cells. *Nature* **573**, 430–433 (2019).
7. Tillmanns, J. et al. Fibroblast activation protein alpha expression identifies activated fibroblasts after myocardial infarction. *J Mol Cell Cardiol* **87**, 194–203 (2015).
8. Urbanska, K. et al. A universal strategy for adoptive immunotherapy of cancer through use of a novel T-cell antigen receptor. *Cancer Res* **72**, 1844–1852 (2012).
9. Butler, A., Hoffman, P., Smibert, P., Papalexi, E. & Satija, R. Integrating single-cell transcriptomic data across different conditions, technologies, and species. *Nat Biotechnol* **36**, 411–420 (2018).
10. Farbehi, N. et al. Single-cell expression profiling reveals dynamic flux of cardiac stromal, vascular and immune cells in health and injury. *Elife* **8**, e43882 (2019).
11. Fu, X. et al. Specialized fibroblast differentiated states underlie scar formation in the infarcted mouse heart. *J Clin Investig* **128**, 2127–2143 (2018).

12. Posey, K. L., Coustry, F. & Hecht, J. T. Cartilage oligomeric matrix protein: COMPopathies and beyond. *Matrix Biol* **71-72**, 161–173 (2018).
13. Reichardt, I. M., Robeson, K. Z., Regnier, M. & Davis, J. Controlling cardiac fibrosis through fibroblast state space modulation. *Cell Signal* **79**, 109888 (2021).
14. Gibb, A. A., Lazaropoulos, M. P. & Elrod, J. W. Myofibroblasts and Fibrosis: Mitochondrial and Metabolic Control of Cellular Differentiation. *Circ Res* **127**, 427–447 (2020).
15. Humeres, C. et al. Smad7 effects on TGF-beta and ErbB2 restrain myofibroblast activation and protect from postinfarction heart failure. *J. Clin. Investig.* **132**, e146926 (2022).
16. Kanisicak, O. et al. Genetic lineage tracing defines myofibroblast origin and function in the injured heart. *Nat Commun* **7**, 12260 (2016).
17. Takemura, G. et al. Role of apoptosis in the disappearance of infiltrated and proliferated interstitial cells after myocardial infarction. *Circ Res* **82**, 1130–1138 (1998).
18. Zhang, Q. et al. Signaling pathways and targeted therapy for myocardial infarction. *Signal Transduct Target Ther* **7**, 78 (2022).
19. Frangogiannis, N. G. Pathophysiology of Myocardial Infarction. *Compr Physiol* **5**, 1841–1875 (2015).
20. Satija, R., Farrell, J. A., Gennert, D., Schier, A. F. & Regev, A. Spatial reconstruction of single-cell gene expression data. *Nat Biotechnol* **33**, 495–502 (2015).
21. Rurik, J. G. et al. CAR T cells produced in vivo to treat cardiac injury. *Science* **375**, 91–96 (2022).
22. Liu, B. et al. TMEM100, a Lung-Specific Endothelium Gene. *Arterioscler Thromb Vasc Biol* **42**, 1495–1497 (2022).
23. Di Benedetto, P. et al. Linking myofibroblast generation and microvascular alteration: The role of CD248 from pathogenesis to therapeutic target (Review). *Mol Med Rep* **20**, 1488–1498 (2019).
24. Opavsky, R. et al. Molecular characterization of the mouse Tem1/endosialin gene regulated by cell density in vitro and expressed in normal tissues in vivo. *J Biol Chem* **276**, 38795–38807 (2001).
25. Jordan, S. C. et al. IgG Endopeptidase in Highly Sensitized Patients Undergoing Transplantation. *N. Engl J Med* **377**, 442–453 (2017).
26. Dick, S. A. et al. Self-renewing resident cardiac macrophages limit adverse remodeling following myocardial infarction. *Nat Immunol* **20**, 29–39 (2019).
27. Kuwahara, K. The natriuretic peptide system in heart failure: Diagnostic and therapeutic implications. *Pharmacol Ther* **227**, 107863 (2021).
28. Schubert, M. L. et al. Side-effect management of chimeric antigen receptor (CAR) T-cell therapy. *Ann Oncol* **32**, 34–48 (2021).
29. Thavapalachandran, S. et al. Platelet-derived growth factor-AB improves scar mechanics and vascularity after myocardial infarction. *Sci. Transl. Med.* **12**, eaay2140 (2020).
30. Watanabe, E. et al. Infarct tissue heterogeneity by contrast-enhanced magnetic resonance imaging is a novel predictor of mortality in patients with chronic coronary artery disease and left ventricular dysfunction. *Circ Cardiovasc Imaging* **7**, 887–894 (2014).
31. Aghajanian, H. et al. Author Correction: Targeting cardiac fibrosis with engineered T cells. *Nature* **576**, E2 (2019).
32. Bagley, R. G. et al. Endosialin/TEM 1/CD248 is a pericyte marker of embryonic and tumor neovascularization. *Microvasc Res* **76**, 180–188 (2008).
33. Li G., et al. Dynamic Molecular Atlas for Cardiac Fibrosis at Single-Cell and Spatial Resolution unveils CD248^{+} fibroblasts in Orchestrating Fibroblast-Immune Interaction. In press. *Nat. Cardiovasc. Res.* https://doi.org/10.1038/s44161-025-00617-1 (2025).
34. Pinto, A. R. et al. Revisiting Cardiac Cellular Composition. *Circ Res* **118**, 400–409 (2016).
35. Chen, A. et al. Spatiotemporal transcriptomic atlas of mouse organogenesis using DNA nanoball-patterned arrays. *Cell* **185**, 1777–1792 e1721 (2022).
36. Tirosh, I. et al. Dissecting the multicellular ecosystem of metastatic melanoma by single-cell RNA-seq. *Science* **352**, 189–196 (2016).

Acknowledgements

We thank Prof. Aidong Chen of Nanjing Medical School for technical support of LV catheterization. This work was supported by the Natural Science Foundation of China [grant number 92068116]; The Science Fund for Distinguished Young Scholars in Jiangsu Province [grant number BK20211501]; The Fundamental Research Funds for the Central Universities [grant number 14380501]. The Basic and Clinical Collaborative Research Promotion Program of Anhui Medical University [grant number 2023xkjT029].

Author contributions

J.X., H.C., and Q.T. conceived the idea and designed the experiments. H.C. and K.H. performed most of the experiments and data analyses. J.W. dissociated and sorted the single cell and performed scRNA-seq data analyses. J.H., N.P., M.G., and Y.J. assisted in the experiments. H.C., J.X., and Q.X. wrote and revised the manuscript. Q.G. and J.C. assisted in revising the manuscript. All authors reviewed and approved the manuscript.

Competing interests

The authors declare no competing interests.

Additional information

Supplementary information The online version contains supplementary material available at https://doi.org/10.1038/s41467-025-56703-2.

Correspondence and requests for materials should be addressed to Qingbo Xu or Jun Xie.

Peer review information *Nature Communications* thanks Mikaël Martino, and the other, anonymous, reviewers for their contribution to the peer review of this work. A peer review file is available.